The Astronomical Journal, 169:263 (26pp), 2025 May https://doi.org/10.3847/1538-3881/adbf0c

The S-PLUS Fornax Project (S+FP): Mapping Globular Clusters Systems within 5 Virial Radii around NGC 1399

Luis Lomelí-Núñez[1], A. Cortesi[1,2], A. V. Smith Castelli[3,4], M. L. Buzzo[5,6,7], Y. D. Mayya[8], Vasiliki Fragkou[1], J. A. Alzate-Trujillo[9], R. F. Haack[3,4], J. P. Calderón[3,4], A. R. Lopes[3], Michael Hilker[6], M. Grossi[1], Karín Menéndez-Delmestre[1], Thiago S. Gonçalves[1], Ana L. Chies-Santos[10], L. A. Gutiérrez-Soto[3], Ciria Lima-Dias[11,12], S. V. Werner[13,14], Pedro K. Humire[15], R. C. Thom de Souza[16,17], A. Alvarez-Candal[18], Swayamtrupta Panda[19,20], Avinash Chaturvedi[21], E. Telles[22], C. Mendes de Oliveira[15], A. Kanaan[23], T. Ribeiro[24], and W. Schoenell[25]

[1] Universidade Federal do Rio de Janeiro, Observatório do Valongo, Ladeira do Pedro Antônio, 43, Saúde CEP 20080-090 Rio de Janeiro, RJ, Brazil
[2] Instituto de Física, Universidade Federal do Rio de Janeiro, 21941-972, Rio de Janeiro, RJ, Brazil
[3] Instituto de Astrofísica de La Plata, CONICET-UNLP, Paseo del Bosque s/n, La Plata, B1900FWA, Argentina
[4] Facultad de Ciencias Astron ómicas y Geofísicas, Universidad Nacional de La Plata, Paseo del Bosque s/n, La Plata, B1900FWA, Argentina
[5] Centre for Astrophysics and Supercomputing, Swinburne University, John Street, Hawthorn VIC 3122, Australia
[6] European Southern Observatory, Karl-Schwarzschild-Strasse 2, 85748 Garching bei München, Germany
[7] ARC Centre of Excellence for All Sky Astrophysics in 3 Dimensions (ASTRO 3D), Australia
[8] Instituto Nacional de Astrofísica Óptica y Electrónica, Luis Enrique Erro 1, Tonantzintla 72840, Puebla, Mexico
[9] Centro de Estudios de Física del Cosmos de Aragón, Spain
[10] Instituto de Física, Universidade Federal do Rio Grande do Sul, Av. Bento Gonçalves 9500, Porto Alegre, RS, Brazil
[11] Instituto Multidisciplinario de Investigación y Postgrado, Universidad de La Serena, Raúl Bitrán 1305, La Serena, Chile
[12] Departamento de Astronomía, Universidad de La Serena, Av. Cisternas 1200, La Serena, Chile
[13] Centre for Extragalactic Astronomy, Durham University, South Road, Durham, DH1 3LE, UK
[14] Institute for Computational Cosmology, Durham University, South Road, Durham, DH1 3LE, UK
[15] Instituto de Astronomia, Geofísica e Ciências Atmosféricas, Rua do Matão, 1226, Cidade Universitária, São Paulo 05508-090, Brazil
[16] Campus Avançado em Jandaia do Sul, Universidade Federal do Paraná, Jandaia do Sul, PR, 86900-000, Brazil
[17] Programa de Pós-graduação em Ciência da Computação, Universidade Estadual de Maringá, Maringá, PR, Brazil
[18] Instituto de Astrofísica de Andalucía, CSIC, Apt 3004, E18080 Granada, Spain
[19] Laboratório Nacional de Astrofísica, MCTI, Rua dos Estados Unidos, 154, Bairro das Nações, Itajubá, MG 37501-591, Brazil
[20] International Gemini Observatory/NSF NOIRLab, Casilla 603, La Serena, Chile
[21] Leibniz-Institut für Astrophysik Potsdam (AIP), An der Sternwarte 16, 14482 Potsdam, Germany
[22] Observatório Nacional, Rua General José Cristino, 77, Bairro São Cristóvão, Rio de Janeiro 20921-400, Brazil
[23] Departamento de Física—CFM—Universidade Federal de Santa Catarina, PO BOx 476, 88040-900, Florianópolis, SC, Brazil
[24] Rubin Observatory Project Office, 950 N. Cherry Avenue, Tucson, AZ 85719, USA
[25] The Observatories of the Carnegie Institution for Science, 813 Santa Barbara Street, Pasadena, CA 91101, USA
Received 2024 December 5; revised 2025 March 4; accepted 2025 March 5; published 2025 April 15

Abstract

We present the largest sample (∼13,000 candidates, ∼3000 of which are bona fide candidates) of globular cluster (GCs) candidates reported in the Fornax cluster so far. The survey is centered on the NGC 1399 galaxy, extending out to 5 virial radii ($R_{\rm vir}$) of the cluster. We carried out a photometric study using images observed in the 12-band system of the Southern Photometric Local Universe Survey (S-PLUS), corresponding to 106 pointings, covering a sky area of ∼208 square degrees. Studying the properties of spectroscopically confirmed GCs, we have designed a method to select GC candidates using structural and photometric parameters. We found evidence of color bimodality in two broadband colors, namely $(g - i)_0$ and $(g - z)_0$, while, in the narrow bands, we did not find strong statistical evidence to confirm bimodality in any color. We analyzed the GCs luminosity functions (GCLF) in the 12 bands of S-PLUS, and we can highlight two points: (a) due to the relatively shallow depth of S-PLUS, it is only possible to observe the bright end of the GCLF and, (b) at that level, in all of the bands, it can be considered to be the log-normal distribution typical for GC systems. With the spatial coverage reached in this study, we are able, for the first time, to explore the large-scale distribution of GCs within and around a galaxy cluster. In particular, we noted that the GCs might be clustered along substructures, which trace the current cluster buildup.

Unified Astronomy Thesaurus concepts: Globular star clusters (656); Galaxy clusters (584); Surveys (1671); Galaxy formation (595); Galaxy evolution (594)

Materials only available in the online version of record: machine-readable table

1. Introduction

Globular clusters (GCs) are among the oldest objects in the Universe, which makes them a key component for understanding the formation and assembly history of galaxies (K. M. Ashman & S. E. Zepf 1998; J. P. Brodie & J. Strader 2006; D. A. Forbes et al. 2018a). Their relatively high luminosities ($M_V = -5$ to -10 mag) and compact sizes (half-light radius of a few parsecs) allow them to be readily detectable in nearby galaxies (W. E. Harris 1996). It has been shown that GC systems of massive galaxies, especially of the metal-rich variety, form through in situ processes and continue assembling during processes of merging or accretion (J. M. D. Kruijssen et al. 2019; M. Reina-Campos et al. 2022). In dense environments such as galaxy clusters, GCs can be associated with individual cluster galaxies or with the intracluster light (J. A. Dawe & R. J. Dickens 1976; D. A. Hanes & W. E. Harris 1986; W. E. Harris 1987; R. E. I. White 1987; M. J. West et al. 1995; L. P. Bassino et al. 2003; B. F. Williams et al. 2007; Y. Schuberth et al. 2008; K. A. Alamo-Martínez & J. P. Blakeslee 2017; M. G. Lee et al. 2022; W. E. Harris & M. Reina-Campos 2024), and can be used to estimate the dark matter content of the galaxy cluster (J. M. Diego et al. 2023; M. Reina-Campos et al. 2023). A variety of GC system properties that are potentially relevant to cosmological theories of galaxy formation have been identified. These include color distribution (S. S. Larsen et al. 2001; M. J. West et al. 2004), luminosity function (L. G. Reed et al. 1994; B. C. Whitmore et al. 1995), radial density distribution (L. P. Bassino et al. 2006; S. S. Kartha et al. 2014), specific frequency as a function of galaxy type (W. E. Harris & S. van den Bergh 1981; E. W. Peng et al. 2008; I. Y. Georgiev et al. 2010), and the nature of their size distribution (A. Kundu & B. C. Whitmore 1998; S. S. Larsen et al. 2001; J. J. Webb et al. 2012). Additionally, over the past two decades, different scaling relations have been found between the GC systems and their host galaxies (e.g., J. P. Caso et al. 2024). These relations associate for instance the total number of GCs ($N_{\rm GC}^{\rm TOT}$) with the masses of supermassive central black holes of their host galaxies (e.g., A. Burkert & S. Tremaine 2010; G. L. H. Harris & W. E. Harris 2011; W. E. Harris et al. 2014; R. A. González-Lópezlira et al. 2017, 2022) and their host galaxy's halo virial mass (e.g., L. R. Spitler & D. A. Forbes 2009; M. J. Hudson et al. 2014; D. A. Forbes et al. 2018b; A. Burkert & D. A. Forbes 2020), offering evidence of a host galaxy–GC–halo connection. The majority of these properties have been exhaustively reviewed in J. P. Brodie & J. Strader (2006), D. A. Forbes et al. (2018a), and M. A. Beasley (2020).

Being the second-nearest rich galaxy cluster, Fornax ($m - M = 31.51$, $\sim$19 Mpc; J. P. Blakeslee et al. 2009) represents a remarkable environment where the processes involved in the formation and evolution of galaxies can be analyzed in detail. In the literature, there are a variety of studies focused on the Fornax cluster, which tackle different aspects of the cluster: the central galaxy NGC 1399 (e.g., E. Iodice et al. 2016), X-ray emission (e.g., C. Jones et al. 1997), dwarf galaxy population (e.g., R. P. Muñoz et al. 2015; Y. Ordenes-Briceño et al. 2018; A. Venhola et al. 2019), ultra-diffuse galaxies (UDGs; e.g., D. Zaritsky et al. 2023), and atomic neutral hydrogen gas (e.g., P. Serra et al. 2023). In particular, the GC system of Fornax has been studied in the past by different authors using both photometric (e.g., M. Kissler-Patig et al. 1997; P. G. Ostrov et al. 1998; L. P. Bassino et al. 2006; J. P. Blakeslee et al. 2012; A. Jordán et al. 2015) and spectroscopic data (e.g., G. Bergond et al. 2007; Y. Schuberth et al. 2010; K. Fahrion et al. 2020; A. Chaturvedi et al. 2022). With photometric GC studies, it is possible to analyze a large number of GC candidates, which enables performing statistical analysis. Yet, in such studies, there is a nonnegligible fraction of contaminants (such as foreground stars and background galaxies). On the other hand, spectroscopic GC studies are much more precise, but they are expensive in terms of telescope observing time, and the total number of recovered GCs is small compared to photometric studies.

Different works were dedicated to the analysis of the GC photometric data from the Fornax Deep Survey (FDS) taken with the Very Large Telescope (VLT) Survey Telescope. For example, E. Iodice et al. (2016) found that the core of the Fornax cluster is characterized by a very extended and diffuse envelope surrounding the luminous galaxy NGG 1399. R. D'Abrusco et al. (2016) reported a density structure in the spatial distribution of GC candidates in a region $\sim$0.5 deg^2 within the core of Fornax. M. Cantiello et al. (2018) obtained surface density maps, color distributions, and radial density profiles of GC candidates around NGC 1399. All of these works studied the GCs around NGC 1399 over a projected area of $\sim$10 deg^2 (e.g., E. Iodice et al. 2016; M. Cantiello et al. 2018). In a recent work, T. Saifollahi et al. (2024), using Euclid (Euclid Collaboration et al. 2022) observations of a 0.5 deg^2 field in the central region of Fornax, identified more than 5000 new GC candidates down to $I_E = 25.0$ mag, about 1.5 mag fainter than the typical turnover magnitude (-7.4 mag in the V band, W. E. Harris 1996; A. Jordán et al. 2007b; D. Villegas et al. 2010) of the GC luminosity function, and investigated their spatial distribution within the intracluster field.

In addition, there are other photometric surveys focused on the Fornax cluster with different objectives such as the Advanced Camera for Surveys Fornax Cluster Survey (ACSFCS; A. Jordán et al. 2007a), the Next Generation Fornax Survey (NGFS; R. P. Muñoz et al. 2015), and the Dark Energy Spectroscopic Instrument (DESI; DESI Collaboration et al. 2024). In particular, the ACSFCS has targeted galaxies with the Hubble Space Telescope (HST) and identified the GCs (e.g., A. Jordán et al. 2015) around them. The NGFS is a deep multiwavelength survey that covers Fornax out to its virial radius (0.7 Mpc; M. J. Drinkwater et al. 2001) and looks at the dwarf galaxies in the central region of the cluster (e.g., P. Eigenthaler et al. 2018; Y. Ordenes-Briceño et al. 2018; E. J. Johnston et al. 2020).

The GCs in Fornax have been objects of different spectroscopic studies, which have focused on confirming them as members of the cluster by estimating their radial velocities (e.g., D. Minniti et al. 1998; Y. Schuberth et al. 2010; A. Chaturvedi et al. 2022), on the determination of ages and metallicities (e.g., M. Kissler-Patig et al. 1998; K. Fahrion et al. 2020), and on the identification of GCs belonging to the intracluster medium (e.g., G. Bergond et al. 2007; Y. Schuberth et al. 2008). In particular, A. Chaturvedi et al. (2022) used spectroscopic data from the Visible Multi Object Spectrograph at the VLT (VLT/VIMOS), covering one square degree around the central massive galaxy NGC 1399, to confirm a total of 777 GCs. Combined with previous literature radial velocity measurements of GCs in Fornax, they compiled the most extensive spectroscopic GC sample of 2341 objects in this environment. They found that red GCs are mostly concentrated around major galaxies, while blue GCs are kinematically irregular and are widely spread throughout the cluster.

Despite the extensive exploration of the GC system in the Fornax cluster using photometric data, all studies have focused on the central regions near NGC 1399 and have been performed in three or four photometric broad bands. In contrast, the Fornax images obtained by the Southern Photometric Local Universe Survey (S-PLUS; C. Mendes de Oliveira et al. 2019), analyzed in the context of the S-PLUS Fornax Project (S+FP; A. V. Smith Castelli et al. 2024), provide coverage of approximately 208 square degrees. This allows for the largest study of GCs in a galaxy cluster to date, extending the study of GCs up to 5 virial radii ($R_{\rm vir}$) along the east–west direction. In a pilot study, M. L. Buzzo et al. (2022) assessed the effectiveness of identifying GCs in the Fornax cluster using S-PLUS images. From the obtained photometry, they applied template fitting techniques to a sample of 115 GCs around NGC 1399 to recover photometric redshifts, as well as ages and metallicities for the GCs. However, it should be stressed that the S-PLUS images are not deep enough ($r \sim 21.30$ mag) to reach the faint end of the GC luminosity function (GCLF).

Apart from Fornax, the GC systems in the Virgo galaxy cluster have also been widely studied (e.g., D. A. Hanes 1977; J. G. Cohen 1988; W. E. Harris 1991). The ACS Virgo Cluster Survey (ACSVCS; P. Côté et al. 2004) is an HST-ACS imaging program of 100 early-type galaxies in the Virgo Cluster. With this data, it was found that the galaxies of the Virgo cluster on average appear to have bimodal or asymmetric GCs color distributions (E. W. Peng et al. 2006); the GCLF turnover is roughly constant in bright galaxies, but it decreases slightly in dwarf galaxies (A. Jordán et al. 2007b). The Next Generation Virgo Survey (NGVS/NGVS-IR; L. Ferrarese et al. 2012; R. P. Muñoz et al. 2014) covers 104 deg^2 in six bands (u^*grizK_s) and extra deep observations in the g band, $g = 25.90$ mag. These data allowed the study of the GC system until the virial radius of the Virgo cluster. In particular, in the spatial distribution of GCs in 100 deg^2, a difference in concentration was found between red (more concentrated) and blue (more extended) GCs over the full extent of the cluster (P. R. Durrell et al. 2014); the possible existence of substructures in the GC population around the Virgo cD galaxy M87 was also found (M. Powalka et al. 2018).

This project aims at studying the Fornax cluster, using the whole S+FP homogeneous data taken through the 12 optical S-PLUS bands. As in A. V. Smith Castelli et al. (2024, hereafter, Paper I) and R. F. Haack et al. (2024, hereafter, Paper II), we consider, for Fornax, a redshift of $z = 0.0048$, taking into account that the systemic velocity of NGC 1399 is $v_r = 1442$ km s^{-1} (N. Maddox et al. 2019). In addition, we assume a distance modulus of $(m - M) = 31.51$ mag for Fornax (J. P. Blakeslee et al. 2009) and, at the corresponding distance, 1$''$ subtends ~0.1 kpc. The mean half mass–radius, r$_e$, of GCs is ~4 pc (S. van den Bergh et al. 1991; A. Jordán et al. 2005; J. J. Webb et al. 2012); therefore, at the Fornax distance, GCs are unresolved sources. With the distance modulus used here, the peak (turnover) of the GCLF in the V band is ~24 mag (e.g., M. Kissler-Patig et al. 1997). We use a cosmology with $H_0 = 70.5$, $\Omega_0 = 0.30$ and $\Omega_l = 0.70$ throughout. In this first paper, we focus on extracting the GC catalog, verifying its effectiveness, and presenting global results. In a following work, we will focus on the detailed study of the GC stellar population properties and their relation with the cluster environment.

The paper is organized as follows. In Section 2 we describe the S-PLUS data used in this study. In Section 3, we present the source detection and photometry. In Section 4, we present the selection method. Results of the completeness tests are also presented. The analysis and discussion of the properties of the GC system are given in Section 5. In Section 6 we give our concluding remarks.

2. S-PLUS Data

The S-PLUS[26] survey will cover ~9300 square degrees of the sky. It uses a robotic ~0.8 m telescope that is located at the Cerro Tololo Inter-American Observatory (CTIO) in Chile (C. Mendes de Oliveira et al. 2019). S-PLUS has a pixel scale of 0$''$.55 pixel^{-1} and a camera field of view (FOV) of ~1.5 square degrees. It uses the Javalambre 12-filter photometric system designed for the Javalambre-Photometric Local Universe Survey (A. J. Cenarro et al. 2019). The filter system is composed of the following seven narrowband filters: J0378, J0395, J0410, J0430, J0515, J0660, and J0861. These map the [O II], Ca H+K, Hδ, G-band, Mgb triplet, and Hα and Ca triplet lines, respectively. The system also includes the u, g, r, i, and z broadband filters (similar to SDSS). In Table 1, we list the S-PLUS filter system.

Table 1
S-PLUS Filter System

Filter	$\lambda_{\rm central}$ (Å)	FWHM (Å)	A_λ/A_V	Comments
(1)	(2)	(3)	(4)	(5)
u	3577	325	1.584	Javalambre u
J0378	3771	151	1.528	[O II]
J0395	3941	103	1.483	Ca H+K
J0410	4094	200	1.434	Hδ
J0430	4292	200	1.364	G-band
g	4774	1505	1.197	SDSS-like g
J0515	5133	207	1.085	Mgb Triplet
r	6275	1437	0.866	SDSS-like r
J0660	6614	147	0.810	Hα
i	7702	1507	0.646	SDSS-like i
J0861	8611	410	0.518	Ca Triplet
z	8882	1270	0.484	SDSS-like z

Note. (1) Filter name. (2) Filter reference wavelength (Å). (3) Filter bandwidth (Å). (4) Milky Way extinction from J. A. Cardelli et al. (1989) (5) Comparison with other filter systems.

The S-PLUS Fornax cluster data are part of the Main Survey (MS) of S-PLUS and cover an FOV of ~20 × 12 square degrees in 106 pointings with the 12 bands. In Figure 1 we show the spatial distribution of all of the sources detected (see Section 3.1) as a cloud of black dots in the 106 pointings delimited by the black squares (~1.4 × 1.4 square degrees). In the center of each FOV, the key name of the S-PLUS pointing is shown, and the red cross represents the coordinates ($\alpha = 54.620941$, $\delta = -35.450657$, J2000 coordinates) of NGC 1399 (E0) galaxy, the most-massive galaxy (10^{13} $\mathcal{M}_\odot$; Y. Schuberth et al. 2010) in Fornax defined as the cluster center. In Appendix A, some important features for the detection of the sources as well as key values of the header for each FOV in the i band are listed. In the 106 pointings, it was possible to detect ~3 million sources. In the next section, we describe the method for the detection and photometry.

The S-PLUS Fornax Project (S+FP) is a collaboration focused on exploiting the 12 bands of S-PLUS covering the Fornax cluster. Two papers have already been published within this framework, A. V. Smith Castelli et al. (2024) and R. F. Haack et al. (2024), and several studies are currently being carried out.

3. Source Detection and Photometry

M. L. Buzzo et al. (2022) studied NGC 1399, the Fornax cluster central galaxy, and assessed the effectiveness of identifying GCs using the first S-PLUS images available. They performed aperture photometry in an area of ~14$'$ × 14$'$ and used four GCs selection criteria (magnitude, concentration index, Gaia proper motion, and template fitting) to select GC candidates. In this work, we increase considerably the area for GC detection in Fornax using 106 FOVs of S-PLUS data, covering an area of ~208 square degrees. Moreover, in this

[26] https://splus.cloud

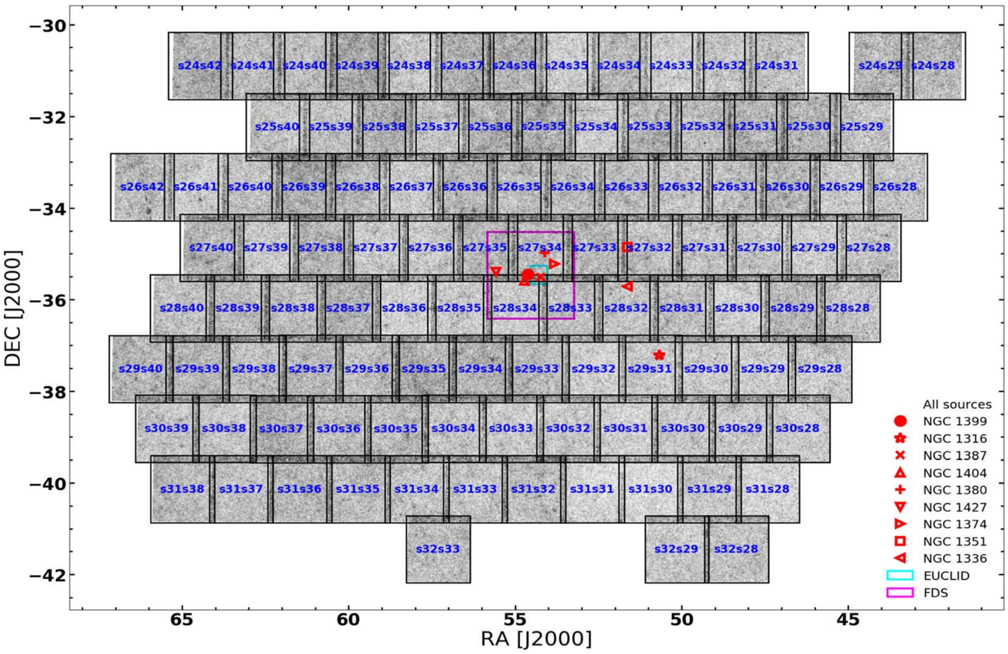

Figure 1. Data coverage of the 106 S-PLUS pointings in Fornax. Cloud of black dots: all detections in each FOV. A total of 3,085,787 sources was detected. A darker color implies a greater number of detected sources. Black solid lines: limits of each pointing. Blue legends: in the center of each pointing, we show their key names from S-PLUS. Red symbols: indicate the central coordinates of some of the brightest galaxies in Fornax. Magenta and cyan squares: represent the FOVs of FDS (E. Iodice et al. 2016) and EUCLID (T. Saifollahi et al. 2024) studies. The image is aligned such that north is up and east is to the left.

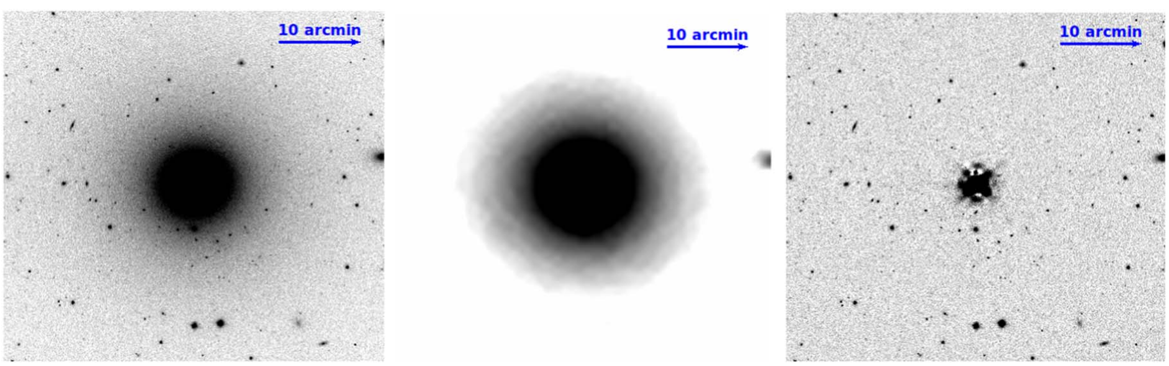

Figure 2. Example of the subtraction of the light profile of the galaxies. Left panel: S-PLUS g-band image of NGC 1399. Center panel: galaxy model. Right panel: residual image. All images are aligned such that north is up and east is to the left.

work, we perform point-spread function (PSF) photometry, specially designed for the detection and measurement of point sources with the characteristics of GCs in Fornax. We also improve the detection and measurement of point sources from the method of Paper II, which is focused on recovering extended sources, like galaxies. In this section, we describe the detection and photometry.

3.1. Source Detection

For source detection and posterior photometric measurements, we used a combination of SExtractor[27] (E. Bertin & S. Arnouts 1996) and PSFEx[28] (E. Bertin 2011). With the objective of recovering the largest amount of GCs that have been confirmed spectroscopically in the literature (A. Chaturvedi et al. 2022), most of which reside within 0.5 R_{vir}, we performed a series of tests with different SExtractor parameters in different runs on test images. These test images were processed to remove the light distribution of the galaxies following different methods. The final detection was performed on images from which their median-filtered version was subtracted, as faint sources are detected more easily in a median-subtracted image (R. A. González-Lópezlira et al. 2017) rather than in the original ones. We perform different tests in the median-filtered images changing the size of the filter (e.g., 3 × 3, 11 × 11, etc.). The best results for recovering sources were obtained using a filter of 41 × 41 pix^2 (Figure 2).

To avoid contamination in the photometric measurements due to the light of the galaxies within the cluster, it is necessary to subtract the light profiles of the galaxies. We performed a series of proofs for obtaining the best modeled background-sky image (Figure 2) using SExtractor, which has the ability of creating SEGMENTATION and BACKGROUND images, among others. Exploiting this capability, we created the background-sky image using different parameters (e.g., BACK_SIZE, BACK_FILTER, BACK_FILTERTHRESH, etc.). We performed various runs of SExtractor testing different parameters (e.g.,

[27] https://www.astromatic.net/software/sextractor
[28] https://www.astromatic.net/software/psfex

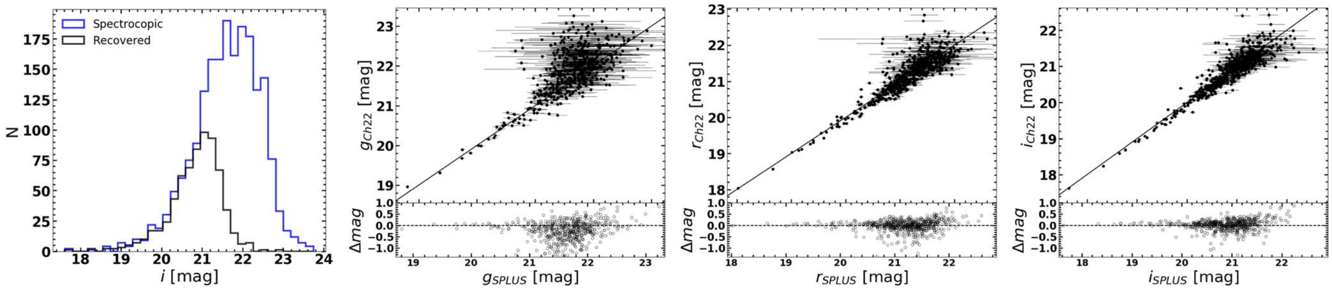

Figure 3. First panel to the left: i-band magnitude distribution of the GC spectroscopic sample from the literature (blue histogram) and GCs recovered with S-PLUS (black histogram). From left to right, we show Fornax GCs PSF magnitude comparison in the g band (second panel), r band (third panel), and i band (fourth panel). In the last three panels, we show the S-PLUS GC magnitudes vs. the spectroscopic GC magnitudes (A. Chaturvedi et al. 2022). The black solid line in the top panels is the identity line, while the black dashed lines in the bottom panels mark where the differences between magnitudes (Δmag = SPLUS − Ch22) are equal to zero.

DETECT_MINAREA=3, 5, 8, DETECT_THRESH=1.5, 2.0, 2.5, BACK_SIZE=16, 32, 64, BACK_FILTER=1, 3, 5 etc.). Finally, we selected the SExtractor parameters (DETECT_MINAREA=3, DETECT_THRESH=1.5, BACK_SIZE=16, BACK_FILTER=3) with which we obtained the best recovery of spectroscopically confirmed GCs and with the lowest scatter in magnitudes compared to the literature (Figure 3).

Compared with the FDS survey data (E. Iodice et al. 2016, $0\farcs21$ pixel^{-1}; and M. Cantiello et al. 2018, $0\farcs26$ pixel^{-1}), the S-PLUS observations have lower-sampling ($0\farcs55$ pixel^{-1}) and are shallower ($r \sim 21.3$ mag for S-PLUS M. L. Buzzo et al. 2022; Paper II; and $r \sim 24.3$ mag for FDS R. D'Abrusco et al. 2016). However, the spatial coverage of the FDS survey is smaller than S-PLUS since it only covers the central FOVs (5 pointings) of S-PLUS in Fornax. For testing the detections in this work, we compare the recovered sample with the spectroscopic GC (spec-GC) catalog of A. Chaturvedi et al. (2022). We recovered ∼1000 out of the total of 2341. In the first panel of Figure 3, we plot the spectroscopic (blue histogram) and S-PLUS recovered samples (black histogram). It is clear that we miss the faint part ($i \gtrsim 22.0$ mag) of the GCLF from the sample of A. Chaturvedi et al. (2022).

3.2. PSF Photometry

PSF photometry is a method to obtain photometry for unresolved or marginally resolved star clusters (e.g., S. C. Gallagher et al. 2010; K. Fedotov et al. 2011; R. A. González-Lópezlira et al. 2017). At Fornax distance (19 Mpc) and considering the S-PLUS pixel scale ($0\farcs55$), GCs (∼50 pc pixel^{-1}) are unresolved sources, given the mean half mass–radius, r_h, of a GCs is ∼4 pc (S. van den Bergh et al. 1991; A. Jordán et al. 2005; P. Barmby et al. 2006; J. J. Webb et al. 2012). Hence, we perform PSF photometry given the characteristics of the GC candidate selection.

The PSF photometry was obtained using a combination of SExtractor and PSFEx, in a similar manner to R. A. González--Lópezlira et al. (2017), L. Lomelí-Núñez et al. (2022), and R. A. González-Lópezlira et al. (2022). A brief description of the procedure is given below:

(a) We performed a first run of SExtractor for detection and selection of point sources based on their brightness versus compactness, as measured by SExtractor parameters MAG_AUTO (a Kron-like elliptical aperture magnitude; R. G. Kron 1980), FLUX_RADIUS (similar to the effective radius), and CLASS_STAR (discriminator between point sources and extended sources). For the PSF creation, in the 106 fields, we selected a similar range in the space MAG_AUTO versus FLUX_RADIUS:
(i) 12 $\lesssim$ MAG_AUTO $\lesssim$ 21.5 mag;
(ii) 1 $\lesssim$ FLUX_RADIUS. $\lesssim$ 2.3 pixel
(iii) CLASS_STAR $\gtrsim$ 0.7
In this range, it was possible to select ∼1000 point sources for the PSF creation in each FOV.

(b) The PSF creation was preformed with PSFEx using the point sources selected in the last step. The spatial variations of the PSF were modeled with polynomials of a degree of 3. To create the PSF, the flux of each star was measured in an aperture of 9 pixel of radius in all bands (equivalent to $4\farcs95 \times 4\farcs95$); such an aperture, determined through the curve of growth method for each passband, is large enough to measure the total flux of the stars, but small enough to reduce the likelihood of contamination by external sources.

(c) We performed a second run of SExtractor using the PSF created in the previous step, for measuring the PSF magnitude (MAG_PSF) and the point and extended sources discriminator, SPREAD_MODEL.

To verify the plausibility of the PSF photometry, we compared the magnitudes measurements with those reported in M. Cantiello et al. (2018) and confirmed spectroscopically by A. Chaturvedi et al. (2022). In the last three panels of Figure 3, we compared the magnitude measurements in three bands: g, r, and i. It was possible to compare 523 (g band), 579 (r band), and 572 (i band) GCs, which have magnitude estimations in both catalogs. In the bottom panels of the last three panels of Figure 3, we show the difference between this work and literature magnitudes, Δmag. The mean and sigma-dispersion for this differences are: $\Delta\bar{\text{mag}} = -0.24$, $\sigma = 0.45$ in g, $\Delta\bar{\text{mag}} = -0.014$, $\sigma = 0.27$ in r, and $\Delta\bar{\text{mag}} = 0.03$, $\sigma = 0.24$ in the i band. Despite being different measurement methods, the estimates are within 1σ of the error, so we can confirm that our PSF photometry is in agreement with the photometry reported in the literature. The higher dispersion values observed in the second panel of Figure 3, i.e., in the g band, are caused by the lower signal-to-noise ratio (SNR) of GCs, intrinsically red objects, in bluer bands, which generates an increase in the uncertainties especially for the faintest objects.

4. Globular Clusters Selection: The Sample of Globular Clusters Candidates

Extracting a catalog of GCs is a challenging task due to the existence of various contaminants, such as foreground stars and background galaxies. For the selection of new GC candidates in the 106 Fornax pointings of S-PLUS, we used SExtractor-derived structural and classifier parameters, FWHM, CLASS_STAR, FLUX_RADIUS, and SPREAD_MODEL, to define an initial cluster sample. This sample has been refined using color–magnitude and color–color diagrams that allowed us to separate foreground stars, background galaxies, and young stellar clusters (YSCs; e.g., B. C. Whitmore et al. 1999, S. S. Larsen 2002, B. C. Whitmore et al. 2023) from old GCs. In addition, we make use of GAIA[29] DATA RELEASE 3 (GDR3) using the tabulated proper-motion coordinates to reject Galactic objects, and finally we estimated the redshift (z) of the remaining objects applying spectral energy distribution (SED) fitting techniques in order to reject background sources.

4.1. Structural Parameters Selection

In the literature, there are a variety of methods for GC candidates selection (e.g., Y. D. Mayya et al. 2008; K. Fedotov et al. 2011; R. P. Muñoz et al. 2014; B. C. Whitmore et al. 2014; R. A. González-Lópezlira et al. 2017; L. Lomelí-Núñez et al. 2022). We used the structural and classifier parameters defined by the spec-GC (A. Chaturvedi et al. 2022) to delimit the selection criteria. The parameters used for the selection are: FWHM, as a discriminator between compact and marginally resolved sources; CLASS_STAR, as a stellarity classifier (compact sources are near 1); SPREAD_MODEL, as another stellarity classifier (compact sources are near 0); and FLUX_RADIUS, as a proxy of the half-light radius (estimation of the size of objects in pixels). Since GCs are bright and well characterized in the i band (see L. Lomelí-Núñez et al. 2022), we set this band to perform the selection. In addition, we imposed that all of the selected sources have an SExtractor $\mathrm{FLAG}_{i\text{-band}} = 0$[30] and MAGERR_PSF $\leqslant$ 0.2 mag in the broad bands (g, r, i, and z).

In Figure 4, we show the parameters FWHM, CLASS_STAR, SPREAD_MODEL, and FLUX_RADIUS versus the i-band magnitude for all of the detected sources (small black points) and the recovered spec-GC sample (yellow circles; A. Chaturvedi et al. 2022). By comparing the parameters of the spectroscopic GCs with those of the detections in the 106 S-PLUS Fornax fields, it is possible to obtain a refined sample of GC candidates. Below we describe the selection criteria:

1. FWHM (top-left panel in Figure 4): we considered all objects with 2.8 pixel $\leqslant$ FWHM $\leqslant$ 9.0 pixel as GC candidates. At the distance of Fornax (19 Mpc, $m - M = 31.51$; J. P. Blakeslee et al. 2009), the pixel scale is 50.6 pc pixel^{-1}.
2. CLASS_STAR (top-right panel in Figure 4): this is a discriminator between point sources (CLASS_STAR $\sim$ 1) and extended sources (CLASS_STAR $\sim$ 0). We chose objects with $0.2 \leqslant$ class $\leqslant 0.90$, where the bulk of the spectroscopic GCs are located.
3. SPREAD_MODEL (bottom-left panel in Figure 4): this is the discriminator between marginally resolved point sources and extended sources provided by the combination of SExtractor with PSFex. From Figure 4, we select the objects displaying SPREAD_MODEL $\leqslant$ 0.015 (see, for example, R. A. González-Lópezlira et al. 2017, 2019, 2022).
4. FLUX_RADIUS[31] (bottom-right panel in Figure 4): this is a proxy of the half-light radius (r_e) estimated by SExtractor. From the comparison between spec-GC sample and all detections in Figure 4, we chose as GC candidates the sources with 1 pixel $\leqslant$ FLUX_RADIUS $\leqslant$ 4 pixel.

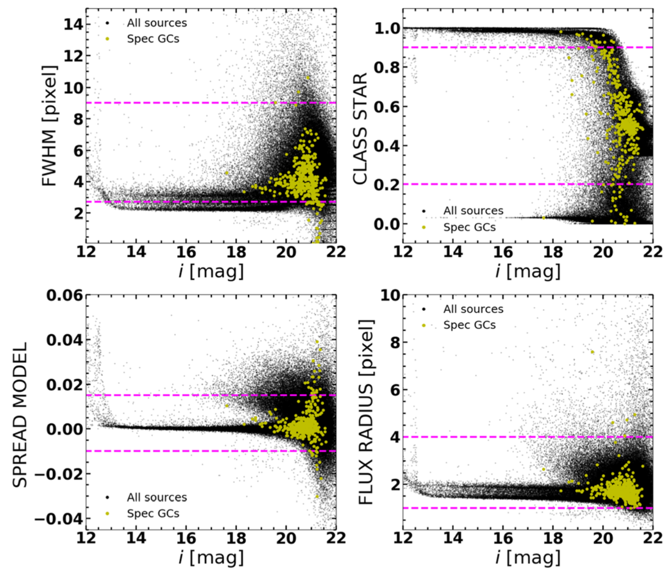

Figure 4. Structural parameters used for the selection vs. i-band magnitude. All detected sources are shown as small black dots, and spec-GC are depicted in yellow. In all panels, the horizontal magenta dashed lines define the selection region of GC candidates.

In this work, we used a combination of CLASS_STAR and SPREAD_MODEL, which is not commonly used in the literature because both parameters are discriminators between point and resolved sources. CLASS_STAR is easier to obtain than SPREAD_MODEL, but the latter is more powerful while requiring a higher computational investment. We selected this method because, by using the combination of both parameters, the number of contaminating sources decreases (see Section 4.7). Finally, after applying the above criteria, we obtained a catalog of 597,634 sources.

4.2. Magnitude Selection

All of the data have been corrected for Galactic extinction ($A_V = 0.039$ mag, $E(B - V) = 0.013$ mag, in direction to NGC 1399) using the values from E. F. Schlafly & D. P. Finkbeiner (2011) provided by the NASA Extragalactic Database.[32] The values are published in the S-PLUS Data Release 4 (DR4; F. R. Herpich et al. 2024).

To avoid the contamination of bright point sources (e.g., galactic stars, ultra-compact dwarf), we select objects displaying $i \geqslant 19.04$ mag ($M_V \sim -11.50$ mag; see transformation equation in Appendix C). The magnitude limit is $\sim$1 mag brighter than that of Omega Cen ($M_V = \sim -10.30$ mag), however, which is in agreement with the spectroscopic sample in which there are GCs with $i \leqslant 19.04$ mag. Considering a

[29] https://www.cosmos.esa.int/web/gaia/dr3

[30] The FLAGS are warnings about the source extraction process. Different values of the FLAG parameter indicate various problems with the photometry (see the SExtractor manual for further explanation; E. Bertin & S. Arnouts 1996).

[31] This is the radius of the circle centered on the light barycenter that encloses half of the total flux.

[32] The NASA/IPA Extragalactic Database (NED) is operated by the Jet Propulsion Laboratory, California Institute of Technology, under contract with the National Aeronautics and Space Administration.

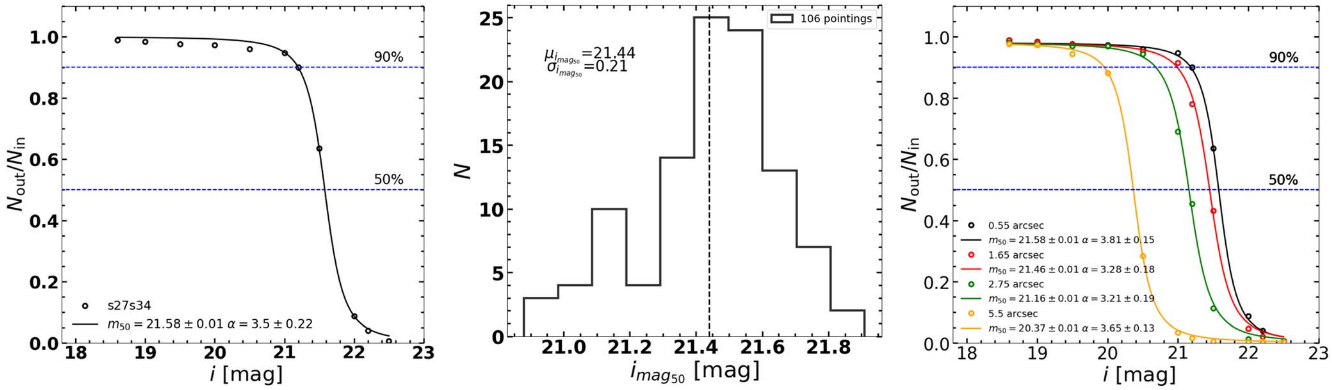

Figure 5. Left panel: example of one completeness curve in the i band for the s27s34 field. The horizontal blue dashed line represents the completeness at the 50% and 90% levels. Center panel: distribution of $i_{\mathrm{mag}_{50}}$ magnitudes recovered for all of the Fornax pointings. The vertical black dashed line represents the mean value of the distribution. Right panel: completeness tests for mock sources with different Gaussian profile sizes: 0″55 (black curve), 1″65 (red curve), 2″75 (green), and 5″5 (yellow curve).

distance modulus of $(m - M) = 31.51$ mag, this magnitude selection corresponds to the 3σ limit of the GC luminosity function assuming $\sigma = 1.40 \pm 0.06$ for massive galaxies (e.g., B. C. Whitmore et al. 1995) and galaxy clusters (e.g., K. A. Alamo-Martínez et al. 2013). For comparison, the dispersion values found for the GCLF of NGC 1399 and the Milky Way (MW) are $\sigma = 1.23 \pm 0.03$ (D. Villegas et al. 2010) and $\sigma = 1.15 \pm 0.10$ (e.g., W. E. Harris 1996; A. Jordán et al. 2007b), respectively.

On the other hand, bias detection exists in all of the astronomical observations toward the faint magnitudes. To ensure the verisimilitude of the observations in the faint part of the GCLF, it is therefore necessary to estimate the completeness magnitude limit. To find out at which magnitude the sample of GC candidates is complete at a 50% level, m_{50}, we carry out completeness tests. In this study, we follow the completeness recipes presented in the works of R. A. González-Lópezezlira et al. (2017), L. Lomelí-Núñez et al. (2022), and R. A. González-Lópezlira et al. (2022). In the next subsections, we present a brief description of the followed procedure.

4.3. Monte Carlo Cluster Simulations

We generated mock GCs using the IRAF/DAOPHOT tasks ADDSTARS and MKOBJETCS. A GC is defined by an intensity profile that follows the PSF obtained in this work and magnitudes in the range 18–23 i-mag considering intervals of 0.5 mag. Around 1300 clusters were generated for each FOV, 100 for each simulated magnitude. The coordinates of these sources were randomly generated and inserted onto an observed S-PLUS image. The same object detection criteria used for real objects were applied on the mock-object added frames.

In the left panel of Figure 5, we show an example of one completeness curve in the i band for one of the central fields, s27s34. In order to quantitatively obtain the magnitude at which the sample is 50% complete, we fitted the points with the Pritchet function (e.g., D. E. McLaughlin et al. 1994; K. A. Alamo-Martínez et al. 2013; R. A. González-Lópezlira et al. 2017, 2022; L. Lomelí-Núñez et al. 2022) given by:

$$f(m) = \frac{1}{2}\left[1 - \frac{\alpha(m - m_{50})}{\sqrt{1 + \alpha^2(m - m_{50})^2}}\right], \tag{1}$$

where α is a fitting constant that determines the curve slope. The function fit values for the s27s34 field are $m_{50} = 21.58 \pm 0.01$ and $\alpha = 3.50 \pm 0.22$. We repeat the same process for the 106 pointings in the i band. In the center panel of Figure 5, we show the magnitude at which the sample is 50% complete in the i band, $i_{\mathrm{mag}_{50}}$, and the distribution of $i_{\mathrm{mag}_{50}}$ for all of the FOVs. We observe that the range of recovered magnitudes spans $\sim$1 mag around the mean of the distribution, $\mu_{i_{\mathrm{mag50}}} = 21.44 \pm 0.21$. The range of magnitudes between $\sim$20.90 and 21.80 that is recovered in the 106 fields is the range of magnitudes in which the sample is 50% complete. The fact that there is a variation of $\mathrm{i}_{\mathrm{mag}_{50}}$ among different tiles may be attributable to different observational conditions such as air masses, exposure times, and number of stacked images (see Appendix A).

Even if GCs at Fornax distance using the S-PLUS data are unresolved objects, we can see in Figure 4 that they can present an FWHM higher than that of the PSF, $\simeq 3$" ($2 \leqslant \mathrm{FWHM} \leqslant 8$), since we are extracting objects at the S-PLUS detection limit (F. R. Herpich et al. 2024). In order to understand the completeness of sources that do not follow the PSF profile, i.e., marginally resolved objects, we performed simulations, where a cluster is defined by an intensity profile that follows a Gaussian function of a given FWHM and a total magnitude (equal to the PSF simulations), with FWHM taking values of 0″55 (black curve), 1″65 (red curve), and 2″75 (green), see Figure 5. In the right panel of Figure 5, we observe that the number of sources detected decreases as we increase the FWHM size, obtaining brighter m_{50} values (e.g., for FWHM = 1″65 and 2″75, $i_{\mathrm{mag}_{50}} = 21.16 \pm 0.01$, and 20.37 ± 0.01, respectively).

4.4. Color Selection

In the bottom panel of Figure 6, we show the Mi_0 versus $(g - i)_0$ color–magnitude diagram (CMD), corrected for Galactic extinction, for the sample of GC candidates selected with the structural parameters plus magnitude criteria (black solid points). The evolutionary loci of the single stellar population (SSP) models from G. Bruzual & S. Charlot (2003) at typical metallicities of YSCs ($Z = 0.008{\sim}1/3$ solar) and GCs ($Z = 0.001$) are shown. These models correspond to synthetic clusters of mass $1 - 5 \times 10^6$ $\mathcal{M}_\odot$ obeying a

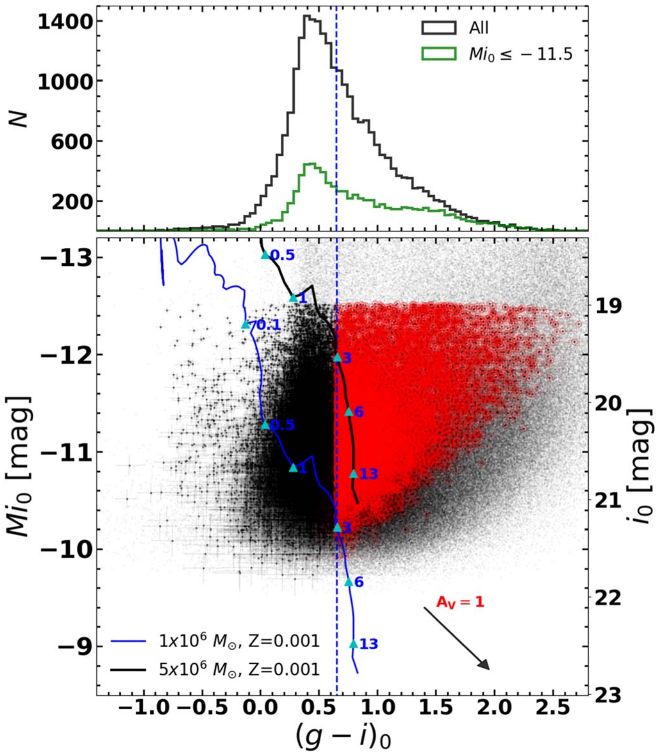

Figure 6. Top panel: color histogram of cluster candidates. The black line shows the color distribution over the entire range of magnitudes, whereas the green histogram shows the distribution for bright ($M_{i_0} \leqslant -11.5$ mag) clusters. The blue dashed vertical line at $(g-i)_0 = 0.65$ mag separates foreground stars, background galaxies, and young cluster candidates from GCs. Bottom panel: M_{i_0} vs. $(g-i)_0$ CMD of all cluster candidates in the 106 Fornax pointings. Sources having $(g-i)_0 \geqslant 0.65$ mag are GC candidates (red small open circles), bluer objects are foreground stars, background galaxies, and young cluster candidates (black points), and all of the detections are represented by a cloud of gray dots. The evolutionary locus of the single stellar population (SSP) models from G. Bruzual & S. Charlot (2003) for a single metallicity $Z = 0.001$, two values of masses of $1 \times 10^6\,\mathcal{M}_\odot$ (blue solid line) and $5 \times 10^6\,\mathcal{M}_\odot$ (black solid line), and a Kroupa initial mass function (IMF), are shown. Locations corresponding to ages of 0.1, 0.5, 1, 3, 6, and 13 Gyr are depicted with cyan triangles in each SSP. The chosen color cut separates clusters older than 3 Gyr from the younger ones for unreddened SSPs. The reddening vector with $A_V = 1$ mag is represented by the black arrow.

Kroupa initial mass function (IMF) between masses 0.1 and 100 $\mathcal{M}_\odot$. In the top panel of Figure 6, we show the $(g-i)_0$ color histogram of all cluster candidates (black histogram) and that of the clusters brighter than $M_{i_0} \leqslant -11.5$ mag (green histogram). For the bright cluster sample, there seems to be a second distribution that peaks at $(g-i)_0 \sim 0.5$ mag. The color that separates the two distributions corresponds to the $(g-i)_0 = 0.65$ mag bin. The blue and red distributions correspond to the unresolved foreground, background contaminants or YSCs in star-forming galaxies, and GCs, respectively. Based on the SSP models and the color distribution, we use $(g-i)_0 = 0.65$ mag to separate GCs from other objects (e.g., N. Hwang & M. G. Lee 2008; L. A. Simanton et al. 2015; L. Lomelí-Núñez et al. 2022; B. C. Whitmore et al. 2023). Different photometric studies used a selection cut in color $(g-i)_0 \sim 0.4$–0.5 mag (e.g., V. Pota et al. 2013; M. Cantiello et al. 2018). However, when compared with the SSP models used here ($Z = 0.001$), such a color is equivalent to 1 Gyr, a very young age to be consistent with old classic GCs. On the other hand, in both panels of Figure 7, we plot the spectroscopically confirmed GCs (yellow circles) by A. Chaturvedi et al. (2022). The total number of GCs in this catalog is 2341. It was only possible to plot 1807 GCs with good photometric estimations, and only approximately 2% have a color $(g-i)_0 \leqslant 0.65$ mag. Taking into account the colors of the spec-GCs, $(g-i)_0$, it is possible to infer that the bulk of the GCs displays $(g-i)_0 > 0.65$ mag (both panels of Figure 7). Therefore, we consider that a color cut $(g-i)_0 \leqslant 0.65$ mag is not suitable for the selection of classic old GCs, since the number of contaminant sources can increase considerably, and the loss of GC candidates is low. On the other hand, in the right panel of Figure 7, we show a color–color diagram, $(r-i)_0$ versus $(g-i)_0$, used for the selection of GC candidates (e.g., V. Pota et al. 2013; S. S. Kartha et al. 2014; V. Pota et al. 2015). The red dots are the GC candidates that meet the criteria described above and display $(r-i)_0 \geqslant 0.19$ mag $\pm 1\sigma$ ($\sim$3 Gyr, $Z = 0.001$). However, in these kinds of color–color diagrams, there is a large number of objects that can contaminate the GC candidates sample. As shown by the SSP (solid lines in colors), in these diagrams, it is difficult to break the age–metallicity degeneracy without using the u band. In Section 4.6, we explain the GC candidate selection using a color–color diagram employing the S-PLUS u band.

Although using the structural parameters we have been able to reject most of the contaminating objects in our sample as Galactic stars or background galaxies, there is a possibility that the GC candidates sample still contains a number of contaminants. In the next subsections, we describe the processes used to obtain a sample much reduced in contaminants.

4.5. Refining the GC Selection through Comparison with DESI and GAIA and the Application of SED Fitting

We cross-matched the GC candidate sample with DESI Legacy Imaging Surveys[33] (hereafter, DESI; DESI Collaboration et al. 2024), which has covered the Fornax cluster, with a pixel scale sampling of 0.20 pix arcsec^{-1} (twice of the S-PLUS resolution) and a photometric depth of 23.4 mag in the r band. With the cross-match, we recovered $\sim$99% of GC candidates, of which we used the DESI object classification ("type"), which includes point sources ("PSF"), round exponential galaxies with a variable radius ("REX"), deVaucouleurs ("DEV") profiles (elliptical galaxies), exponential ("EXP") profiles (spiral galaxies), and Sérsic ("SER") profiles. Ultimately, we retain only the objects classified as "PSF" and "REX" ($\sim$60%). In fact, cross-matching the A. Chaturvedi et al. (2022) spectroscopic catalog with the light profile classification provided by DESI, we found that the GCs were primarily classified as "PSF" ($\sim$68%), then as "SER" (15%), "DEV" (7%), and finally "EXP" (2%). Therefore, considering only objects classified as "PSF" might exclude real GC candidates. At the same time, from a visual inspection and profile examination (using IRAF/IMEXAM), we concluded that the "REX" objects on average had a similar profile to "PSF" objects, while the "SER" objects presented extended profiles.

[33] The DESI Legacy Surveys team is producing an inference model of the extragalactic sky in the optical and infrared. The original Legacy Surveys (MzLS, DECaLS, and BASS) conducted dedicated observations of $\sim$14,000 square degrees of extragalactic sky visible from the northern hemisphere in three optical bands (g,r,z), which was augmented with four infrared bands from NEOWISE.

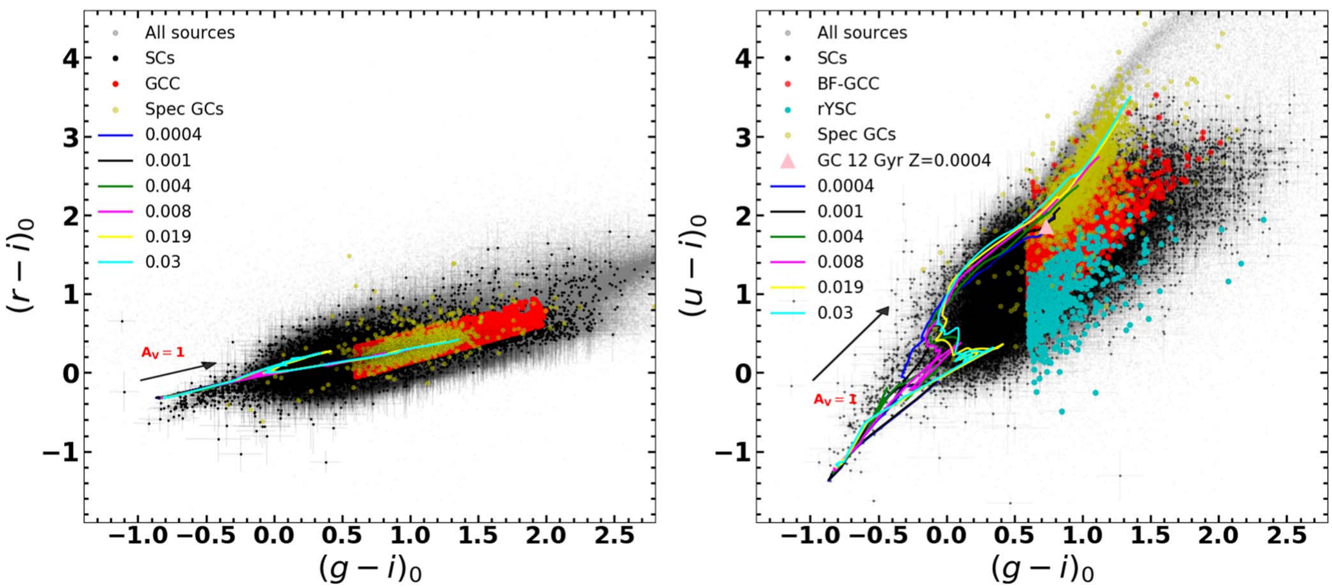

Figure 7. Left panel: color–color diagram $(r - i)_0$ vs. $(g - i)_0$ of all cluster candidates (SCs, black dots). Sources having $(g - i)_0 \geqslant 0.65$ mag and -0.10 mag $\leqslant (r - i)_0 \leqslant 0.70$ mag are considered GC candidates (GCC, red dots). The chosen color cut separates clusters older than 3 Gyr from the younger ones for unreddened SSPs. Right panel: color–color diagram $(u - i)_0$ vs. $(g - i)_0$ showing the u-selected cluster candidates (SCs). Objects displaying $(g - i)_0 \geqslant 0.65$ mag are GC candidates (BF-GCC, red dots), and bluer objects are possible young star cluster candidates (rYSC, black dots). The bluest color that a classical GC can have (corresponding to $Z = 0.0004$ and to an age of 12 Gyr) is marked by a rose solid triangle ($(g - i)_0 \sim 0.6$ and $(u - i)_0 \sim 1.9$). The reddened young star clusters that displays colors typical of GCs are contaminants and are identified by open cyan circles. In both panels: the reddening vector with $A_V = 1$ mag is represented by the black arrow. The evolutionary loci of SSPs from G. Bruzual & S. Charlot (2003) for different metallicities using a Kroupa IMF are shown by solid curves of different colors, following the color notation shown in each panel. The spectral GCs (spec-GC) are depicted by yellow circles.

We also used the GAIA[34] catalog (Gaia Collaboration et al. 2016) to reject local contaminant sources. In order to separate Galactic stars from other objects, we used the proper motions from the catalog provided by Gaia Data Release 3 (Gaia DR3; Gaia Collaboration et al. 2021) centered in NGC 1399 with coverage of all of the Fornax field of S-PLUS. The number of sources of the Gaia catalog in the Fornax area is 1,129,284. We use the SNR of the proper motion (SNR$_\mu$; K. T. Voggel et al. 2020, M. L. Buzzo et al. 2022),

$$\mathrm{SNR}_\mu = \sqrt{\mu^2_{\mathrm{R.A.}} + \mu^2_{\mathrm{decl.}}} \Big/ \sqrt{\sigma\mu^2_{\mathrm{R.A.}} + \sigma\mu^2_{\mathrm{decl.}}}, \tag{2}$$

to select stars. Here, μ is the proper motion, and $\sigma\mu$ is the dispersion in each coordinate. In fact, nonstellar objects are expected to have proper motions that are consistent with 0 at the 3σ confidence level, while genuine stars are expected to have SNR$_\mu >$ 3. We performed a cross-match between Gaia proper motions and our catalog, with which it was possible to reject $\sim$50% of GC candidates. The error for the cross-match was the mean of the (RA,DEC) coordinate errors from the Gaia catalog ($\sim 0\farcs7$).

We used LEPHARE[35] (S. Arnouts et al. 2002), to reject extragalactic contaminant sources. LEPHARE is a software of template fitting (TF) based on a χ^2 minimization, to fit data with both galactic and stellar templates. The templates used for this analysis are a set of galactic SEDs derived by the COSMOS survey collaboration (N. Scoville et al. 2007), and the Pickles stellar spectra library (A. J. Pickles 1998). We used physically motivated priors to perform the LEPHARE fitting: $(g - i)$ color, absolute magnitude in the i band (M_i), extinction, and redshift $z = 0.4$, considering that the photometric redshift distribution of S-PLUS sources with $r < 22$ mag peaks at $z = 0.2$ (C. R. Bom et al. 2024). In Figure 8, we show the redshift results from the SEDs fitting for the sample before GAIA rejections (black solid line), after GAIA rejections (blue solid line), and the sample of bona fide GC candidates (BF-GCC; see Section 4.6, red solid line). We show the velocity of NGC 1399, $v_* = 1424.91 \pm 3.90$, $z_* = 0.00475 \pm 0.00001$ (black dashed line; A. W. Graham et al. 1998), and the range for the z estimations, $z - \sigma$ (blue dashed line) and $z + \sigma$ (red dashed line), where σ is the mean error. We observed that $\sim$99% of the distributions fall within the estimated range. The final catalog of GC candidates consists of 12,999 objects. In Table 2 we list all of the selection criteria.

4.6. Contamination of the GC Sample from Reddened Young Star Clusters, Stars, and Galaxies

GCs' color is the most useful discriminator between young and old GC populations. For example, metal-poor SSPs ($Z \leqslant 0.001$) predict $(g - i) \geqslant 0.65$ mag for populations older than $\sim$3 Gyr (G. Bruzual & S. Charlot 2003). The use of color–color diagrams involving ultraviolet and optical filters is known to break the age–metallicity degeneracy (e.g., I. Y. Georgiev et al. 2006; N. Bastian et al. 2011; K. Fedotov et al. 2011; L. Lomelí-Núñez et al. 2022, B. C. Whitmore et al. 2023). The evolutionary loci of clusters in such a color–color diagram for theoretical SSPs from G. Bruzual & S. Charlot (2003) of different metallicities, have been shown in Figure 7. There, we plot all of the sources selected with the structural parameters and magnitude cuts (see Sections 4.1 and 4.2) as black dots, while sources that also meet with the distance selection criteria (GAIA-LEPHARE selection) and DESI classification (see Section 4.5) are shown as red and cyan open circles.

[34] https://gea.esac.esa.int/archive/
[35] http://www.cfht.hawaii.edu/~arnouts/lephare.html

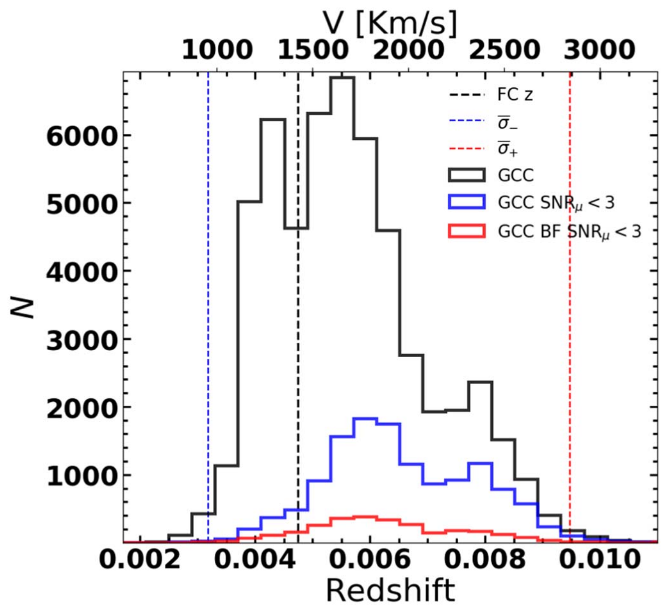

Figure 8. Redshifts estimated with LEPHARE. Black solid line: sample of GC candidates before DESI and GAIA rejections. Blue solid line: sample after DESI and GAIA rejections. Red solid line: sample of bona fide GC candidates. Black dashed line: the redshift of NGC 1399, the dominant galaxy of Fornax. Blue and red dashed lines: lower and upper range taking into account the mean errors for the redshift estimations.

Table 2
GC Candidates Selection Resume

Parameter (1)	Value (2)	$N_{\rm GCC}$ (3)
All	⋯	~3 million
FWHM	$2.8 \leqslant$ FWHM $\leqslant 9.0$ [pixel]	⋯
CLASS_STAR	$0.2 \leqslant$ CLASS_STAR $\leqslant 0.9$	⋯
SPREAD_MODEL	SPREAD_MODEL $\leqslant 0.15$	⋯
FLUX_RADIUS	$1 <$ FLUX_RADIUS $\leqslant 4$ [pixel]	~500,000
MAG_PSF	$19.5-1.0\sigma \leqslant i \leqslant$ mag$_{50}$ [mag]	
MAGERR_PSF	g,r,i,z-bands $\leqslant 0.2$ [mag]	⋯
$(g-i)_0$	$(g-i)_0 \geqslant 0.65 \pm 1.0\sigma$ [mag]	⋯
$(r-i)_0$	$(r-i)_0 \geqslant 0.19 \pm 1.0\sigma$ [mag]	⋯
$(u-g)_0$	$(u-g)_0 \geqslant 1.05 \pm 1.0\sigma$ [mag]	~50,000
Gaia pm	SNR$_\mu$<3	⋯
TF$_{\rm crit}$	$\chi^2_{\rm red}$(galactic)<$\chi^2_{\rm red}$(stellar)	~25,000
DESI	"type" classification	12,999
BF-GCC	⋯	2643

Note. (1) Selection parameter. (2) Selection cut. (3) Number of objects selected for cut. Note that not all rows have a number specified, as certain cuts are made simultaneously.

The $(u-i)$ colors of reddened young (<10 Myr) clusters are distinctly different from that of clusters older than ~3 Gyr, which allows us to break the age–reddening degeneracy. Thus, possible background galaxies and reddened YSCs (contaminants) would lie below the SSP locus for age >3 Gyr having a bluer $(u-i)$ color for a given $(g-i)$. In other words, for a redder, $(g-i) > 0.65$ mag, cluster to be considered as a genuine GC, its $(u-i)$ color, after taking into account photometric errors, should correspond to a location above the SSP locus in Figure 7. As illustrated in Figure 6 of L. Lomelí-Núñez et al. (2022), the real errors in photometry are larger than the formal error bars, which limits the use of the colors for a precise determination of age. Nevertheless, the photometric quality is good enough to separate background galaxies and reddened YSCs from GCs. Finally, from Figure 7, we can select the sample of bona fide GC candidates (BF-GCC) as all sources (red empty circles) that meet all of the selection criteria, and it is also possible to obtain a sample of possible reddened YSCs (cyan open circles).

We obtain a mean estimation of stars and background galaxies contaminants in the final sample. The size of the region that we are analyzing is large, so we randomly selected 12 regions from the center to the outermost zones, in which there is a high, medium, and low density of detected sources. We used the Besançon model of the Galaxy (A. C. Robin et al. 2003) to estimate which fraction of sources corresponds to foreground stars in the Milky Way. In the panels of Figure 9, we show the i_0 versus $(g-i)_0$ CMD in three selected fields, which have high (left), medium (center), and low (right) crowding, where the clouds of black dots are all of the detections in each pointing. The blue circles are the observed stars, green circles are the expected stars from Besançon models, and red circles are the BF-GCC. The observed stars were selected using a typical value of CLASS_STAR > 0.90 and SNR$_\mu$, and for contamination estimation, we used the stars that meet the selection criteria (colors and magnitudes) for GC candidates. The modeled stars are restricted to the selection parameter space, which is the reason they are overlapping with the observed stars. We estimate the percentage of contaminating objects as the difference between the recovered stellar objects and the objects predicted by the Besançon model divided by the number corrected for incompleteness of candidate GCs. We obtained a mean value of point-source contaminants of ~29%. We repeat the same procedure in the $(u-i)_0$ versus $(g-i)_0$ color–color diagram, where the mean value of contaminants is ~20%.

4.7. Second Contaminants Estimation Test

As a final test, in order to estimate the number of contaminants (foreground stars and background galaxies) in our sample, we used a control field (CF) from the S-PLUS data at high Galactic latitudes, to reduce the contribution from Milky Way sources, avoiding lines of sight with known nearby galaxies. The CF is SPLUS-s46s27 with central coordinates R.A.$_{\rm J2000}$ = 68.32, decl.$_{\rm J2000}$ = −59.53. The Galactic extinction value in that direction is $A_V = 0.033$ (E. F. Schlafly & D. P. Finkbeiner 2011).

In Figure 10 we show the comparison between three structural parameters in the $(g-i)_0$ versus $(u-i)_0$ color–color diagram for one Fornax field (FF, left panels) and the CF (right panels). In all of the panels, the sources depicted by black open circles are the objects that meet the GC candidates selection criteria in the parameters SPREAD_MODEL CLASS_STAR and FWHM. In this example, the number of GC candidates in the CF is considerably smaller than in the Fornax field for each of those structural parameters. The objects that meet the selection criteria in the CF are considered possible contaminants (column (3) in Table 3). The percentage of contaminants in each structural parameter will be the ratio of the number of objects in the CF divided by the number of objects in the FF (column (4) in Table 3). Thus, the percentages of possible contaminants per structural parameter are 15% (SPREAD_MODEL), 19% (CLASS_STAR), and 21% (FWHM). We emphasize that in the selection of GCs, we are using the

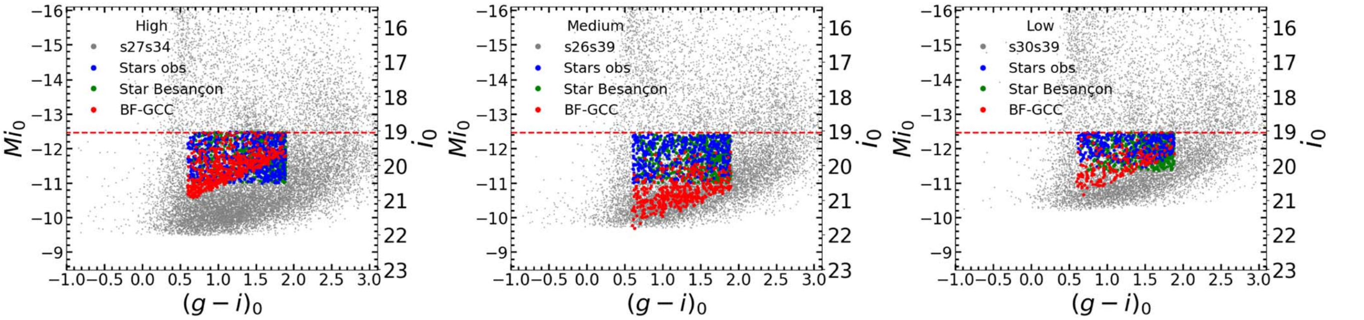

Figure 9. Contaminants estimation in the i_0 vs. $(g-i)_0$ CMD in three selected fields, which have high (left), medium (center), and low (right) crowding. The cloud of black small dots is all of the detections in each pointing. Blue circles are the observed stars (sources with CLASS_STAR > 0.90), green circles are the expected stars from Besançon models (A. C. Robin et al. 2003), and red circles are the BF-GCC. Red dashed line represents the bright selection limit in magnitude, which is estimated using the turnover of the GCLF (see Section 4.2).

combination of structural parameters, so when using the combination of these parameters, the percentage of contaminants in this field is reduced by up to 11% (11/103). We follow the same procedure in 12 randomly selected fields, finding the mean values of contaminants per structural parameter of 27% (SPREAD_MODEL), 27% (CLASS_STAR), and 30% (FWHM), while the mean value of contaminants using the combination of all of the structural parameters was 18%. In Table 3, we show the numbers (columns (2) and (3)) and percents (column (4)) in all of the FOVs where we estimated the contamination.

To ensure the genuineness of our BF-GCC sample, we performed two additional tests: a comparison of our sample with galaxy catalogs from the literature, and a visual inspection. In order to discard contamination for galaxies, we compared our BF-GCC sample with a compilation of 1005 Fornax galaxies reported in the literature (see Paper I). When performing a coordinate cross-match with an error of up to 10″, we obtained seven matches with our catalog. We also compared the BF-GCC sample with the compilation of UDGs from D. Zaritsky et al. (2023), obtaining four matches, three of which are among the seven matches with the Fornax galaxies compilation. Finally, we compared the BF-GCC sample with the catalog of 61 nucleated dwarf galaxies from Y. Ordenes--Briceño et al. (2018), with a similar coordinate error, resulting in no match in this case. As a next step, we performed a visual inspection of each one of the objects. With this last inspection, we rejected ∼50 objects that had a large extended emission and objects contaminated by other sources. The total number of objects in the BF-GCC sample is 2643. After the entire selection process, we have created a BF-GCC sample with a low number of contaminants (∼20%), in which we perform further analysis in the following sections.

In summary, we used SExtractor for detecting ∼3 million sources, and we used structural and classifier parameters (FWHM, CLASS_STAR, etc.) as a first discriminating step, obtaining a sample of ∼500,000 sources. The next discriminator was the i-band magnitude and colors $(g-i)_0$ and $(r-i)_0$, from which we obtained a subsample of ∼50,000 sources. Then we used DESI classification, GAIA and LEPHARE, to reject Galactic and extragalactic contaminants from which we obtained a subsample of ∼13,000 sources (flag=00 in Table 4). Finally, using the $(u-i)_0$ color, we separated the young reddened stellar clusters (flag=01 in Table 4) and selected the BF-GCC sample (flag=02 in Table 4), resulting in 2643 sources. In Table 4 we list the 10 brightest BF-GCCs, presenting their names (column (1)), coordinates (columns (2)–(3)), i-magnitudes (column (4)) broadband colors (columns (5)–(8)), structural parameters (columns (9)–(12)), absolute i-magnitude (column (13)), and flag classification (column (14)), as an example of the fully published table. In the next section, we present the results of the analysis of the properties for the BF-GCC sample.

5. Properties of the Globular Cluster System: Results and Discussion

We emphasize that one of the great strengths of S-PLUS is the large spatial coverage combined with its 12-band filter system, which allows us to perform statistical estimations over large sky areas. Having obtained a sample of BF-GCs in the 106 Fornax pointings, the next natural step is analyzing their photometric properties. In the following sections, we present the analysis of their color distributions, the GCLFs, and the spatial distribution, respectively. All magnitudes and colors have been corrected for the foreground Galactic extinction using the A_V values given in Table 1, and the J. A. Cardelli et al. (1989) reddening curve.

5.1. Color Distributions

Previous studies (e.g., L. P. Bassino et al. 2006, H.-S. Kim et al. 2013, M. Cantiello et al. 2018) have shown that the color distribution of the GC system in Fornax is bimodal. However, they have been focused on the central region of the Fornax cluster, where NGC 1399 is located, and they cover, at most, one virial radius; they are also much deeper, sampling GCs of typical GC masses, i.e., $10^5\ \mathcal{M}_\odot$. Here we show that the color bimodality of the GC system is evident up to, at least, 3 $R_{\rm vir}$ (see Section 5.3.2). A common result found in early-type galaxies is a bimodal distribution of GCs colors (S. E. Zepf & K. M. Ashman 1993, K. Gebhardt & M. Kissler-Patig 1999, S. S. Larsen et al. 2001). A correlation between color and metallicity was also observed in different galaxies (e.g., E. W. Peng et al. 2006; A. Alves-Brito et al. 2011). Given this correlation, the bimodal color distribution has been attributed to a bimodality in the abundance of metals (see, J. P. Brodie & J. Strader 2006). The bimodality would indicate the presence of two different populations of GCs: the metal-poor (commonly referred to as blue) and the metal-rich (usually designated as red). The two kinds of GCs also seem to be spatially segregated, with the distribution of metal-poor GCs having a larger scale length as compared to the metal-rich GCs (e.g., S. S. Larsen & J. P. Brodie 2003; Y. Schuberth et al. 2010; J. J. Webb et al. 2012; S. S. Kartha et al. 2014).

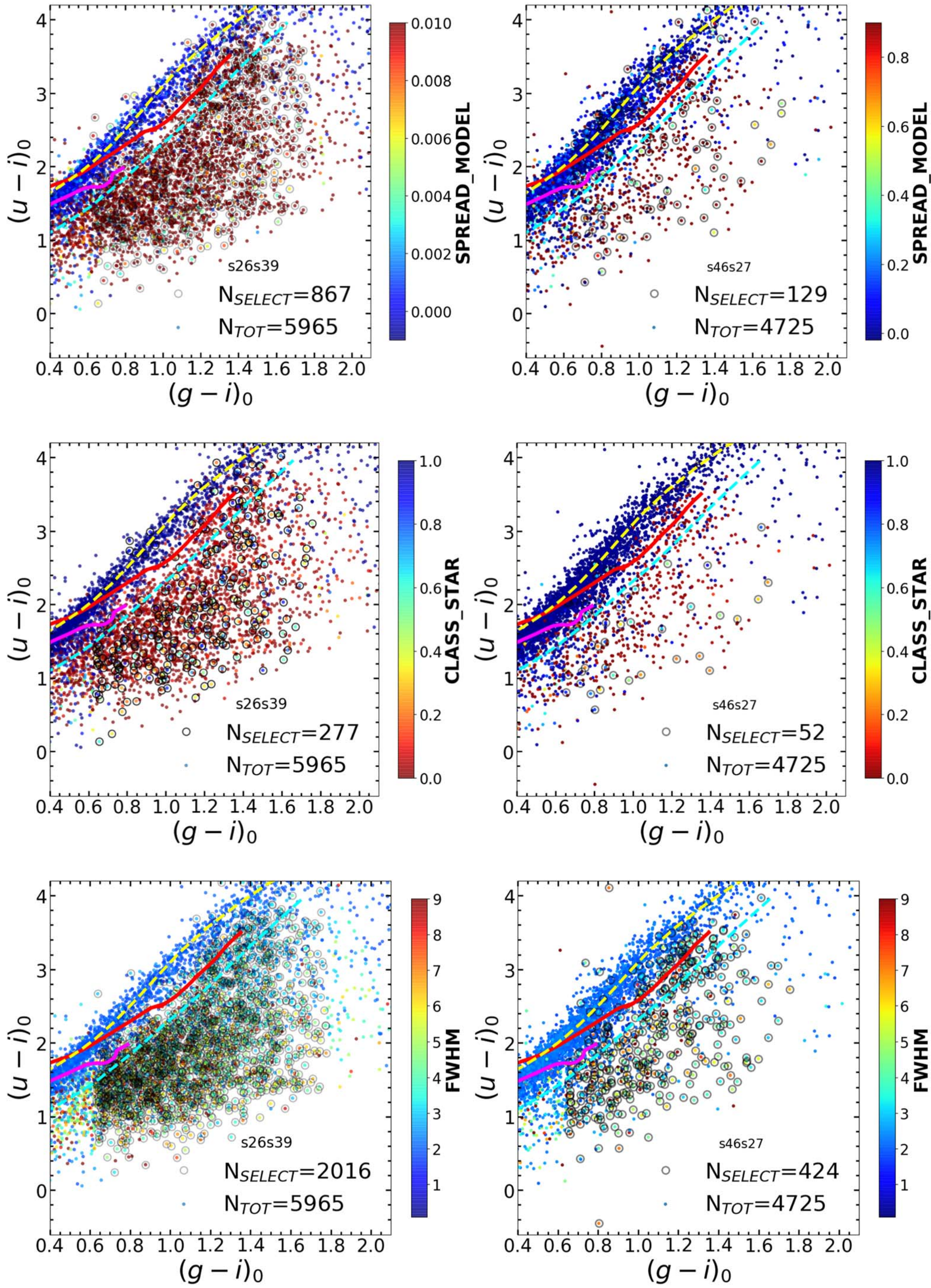

Figure 10. Contaminants estimation in the $(u - i)_0$ vs. $(g - i)_0$ color–color diagram. Comparison of structural parameters in the S-PLUS-s26s39 Fornax field (left panels) and in the S-PLUS-s46s27 control field (right panels). From top to bottom, we show SPREAD_MODEL × 100, CLASS_STAR, and FWHM. $N_{\rm TOT}$ are all of the objects present in each FOV (small colored dots), and $N_{\rm SELECT}$ are the objects that meet with the selection criteria (small colored dots into black open circles), respectively. The magenta and red lines sketch the loci of SSPs models with $Z = 0.0004$ and $Z = 0.03$, respectively. The cyan and yellow lines sketch the loci of zero-age main sequence (ZAMS) stars with $Z = 0.0001$ and $Z = 0.04$, respectively.

In Figure 11 we show the $(g - i)_0$ color distributions for the BF-GCC sample where the subindex 0 stands for Galactic reddening-corrected colors, using the A_V values in Table 1. In total, we analyzed 10 colors with the broad bands: $(u - g)_0$, $(u - r)_0$, $(u - i)_0$, $(u - z)_0$, $(g - r)_0$, $(g - i)_0$, $(g - z)_0$, $(r - i)_0$, $(r - z)_0$, and $(i - z)_0$ and 15 colors with the narrow bands: $(\rm J0378 - J0410)_0$, $(\rm J0378 - J0430)_0$, $(\rm J0378 - J0515)_0$, $(\rm J0378 - J0660)_0$, $(\rm J0378 - J0861)_0$, $(\rm J0410 - J0430)_0$, $(\rm J0410 - J0515)_0$, $(\rm J0410 - J0660)_0$, $(\rm J0410 - J0861)_0$, $(\rm J0430 - J0515)_0$, $(\rm J0430 - J0660)_0$, $(\rm J0430 - J0861)_0$, $(\rm J0515 - J0660)_0$, $(\rm J0515 - J0861)_0$, and $(\rm J0660 - J0861)_0$. In Section 5.3, we analyzed the $(g - i)_0$ and $(g - z)_0$ color distributions at differents $R_{\rm vir}$ from the center of Fornax.

To confirm the presence of bimodality in the color distributions, we used the Gaussian mixture modeling (GMM) code (A. L. Muratov & O. Y. Gnedin 2010), which carries out a robust statistical test for evaluating bimodality, and uses a likelihood ratio to compare the goodness of fit for

Table 3
Number of Contaminants per Structural Parameter

Parameter (1)	FF (2)	CF (3)	CF/FF (4)
SPREAD_MODEL	5667	1400	24%
CLASS_STAR	2445	572	23%
FWHM	17036	4664	27%
All	…	…	18%

Note. (1) Parameter of selection. (2) FF, Fornax field. (3) CF, control field. (4) Ratio between CF and FF. "All" denotes the percent of contaminants using all of the selection criteria in all of the fields.

double-Gaussian versus a single Gaussian. This method is independent of the binning of the sample. The results from the GMM test in the color distributions are shown in Table 6 of Appendix B. For a distribution to be considered bimodal, the Kurtosis must be negative, the distance between the peaks of the distributions (D) must be $D > 2$, and p-values must be small (e.g., A. L. Muratov & O. Y. Gnedin 2010). According to GMM results and visual inspection, we find evidence of color bimodality in the colors $(g - i)_0$ and $(g - z)_0$, while we did not find strong statistical evidence to confirm bimodality in any of the narrowband colors. A possible explanation for that might be linked to the fact that the narrowband filters sample a short spectral range. In addition, the larger errors in the narrowband magnitude estimations might extend the color distribution, fading the bimodality. Moreover, we are looking at only very bright (massive) GCs. The blue tilt found for bright (massive) GCs washes out a color bimodality for massive GCs (e.g., S. Mieske et al. 2010; J. Fensch et al. 2014).

In Table 5 we present the BF-GCC candidates divided in blue and red subpopulations using $(g - i)_0 = 0.86$ (columns (3) and (4)) and $(g - z)_0 = 1.24$ (columns (5) and (6)) according to GMM results, which are in agreement with the values found in R. D'Abrusco et al. (2022) for NGC 1399. We will use this classification in order to analyze the projected distribution of the BF-GCC in the rest of the colors. In Figure 12, we show one example of these novel color–color diagrams using colors different to those used for the GC candidates selection (see Section 4.4). From the SSP metal-poor model shown in Figure 7, we set the color cut selection of GC candidates with a minimum age of $\sim$3 Gyr. When compared with Figure 12, it is observed that the sample of BF-GCC remains older than >1 Gyr ($Z = 0.001$, black star). In the $(g - z)_0$ versus $(r - z)_0$ diagram, $\sim$20% (453 objects) of the blue subsample displays an age $\lesssim$3 Gyr ($Z = 0.001$, black square), while $\sim$53% (1086 objects) is older than 12 Gyr ($Z = 0.001$, black triangle). On the contrary, 99% of the red subsample seems to be older than 12 Gyr ($Z = 0.001$, black triangle).

There are two possible explanations for this: the projected color shift in the BF-GCC toward ages younger than 3 Gyr can be attributed to the fact that in the color selection we accept objects with 1σ photometric errors; or according to this brief analysis, independently of selection cuts, the blue subsample appeared to have more than one formation peak, a portion older than >12 Gyr, formed in a first burst of star formation (K. M. Ashman & S. E. Zepf 1992), or invoking the mass–metallicity relationship (P. Côté et al. 1998; J. Strader et al. 2005; D. A. Forbes & R.-S. Remus 2018), formed in less-massive satellite galaxies that are subsequently acquired by giant galaxies during the accretion process. The other portion of the GCs was probably formed in a more recent burst $\sim$2–3 Gyr, which would then not be old classical GCs, but rather intermediate-age clusters (e.g., L. A. Simanton et al. 2015). Meanwhile, without taking into account intrinsic extinction, the red subsample is entirely older than >12 Gyr.

In Figure 12, we show the contours that represent the probability (estimated with GMM) for a BF-GCC to be blue (left color bar) or red (top color bar). The loci of both populations together with the probability bars reinforce the hypothesis of the existence of two independent subpopulations.

5.2. GCLFs

Studies have shown that the GCLF for early-type galaxies is universal (e.g., B. C. Whitmore et al. 1995; J. P. Brodie & J. Strader 2006; A. Jordán et al. 2007b; L. Lomelí-Núñez et al. 2022), which implies that the peak of the distribution, or turnover (TO), is the same in all galaxies. This has led many authors (e.g., T. Richtler 2003; D. A. Forbes et al. 2018b) to assume that GC systems are fundamental pieces to understand the formation and evolution processes of their parent galaxies. By understanding the formation processes of individual galaxies, we could understand the formation and evolution processes of galaxy clusters. However, the universality of the GCLF for late-type galaxies has not been fully tested. Examples of studies where universality has been proven are found in the MW (e.g., W. E. Harris 1996; E. Bica et al. 2003), M31 (e.g., M. B. Peacock et al. 2010; S. Wang et al. 2019, suggest a second peak in the GCLF), and a few nearby galaxies (see L. Lomelí-Núñez et al. 2022). Here we show the global GCLF in all observed fields, which may include GC systems in all kinds of galaxies (elliptical, spiral, dwarf, etc.). Subsequent studies will concentrate on the analysis of individual galaxies in Fornax.

In Figure 13, we show the GCLF (black solid histogram) in the i band for the BF-GCC sample. For completeness, we show the 12 bands GCLFs in Figure 18 of Appendix D. We emphasize that it is only possible to observe the brightest part of the GCLF because the S-PLUS images are not deep enough to detect, in a confident manner, objects fainter than $i \sim 21.44$ mag. Thus, it is not possible to observe the TO generally found in early-type galaxies (e.g., B. C. Whitmore et al. 1995). However, it is possible to estimate the expected TO in the i band according to the SSP models from G. Bruzual & S. Charlot (2003), for an old stellar population (12 Gyr) with a low-metal content ($Z = 0.0004$), for which $(g - i)_{AB} = 0.7307$ mag. From the transformation equation for metal-poor stars by K. Jordi et al. (2006; see Appendix C), the TO at $M_V = -7.4 \pm 0.10$ mag (e.g., W. E. Harris 1996; A. Jordán et al. 2007b) translates into a TO at $M_i = -8.3 \pm 0.10$ mag. Considering that $(m - M) = 31.51$ mag for Fornax, the TO is expected to occur at $i = 23.21$ mag. The red dashed line in Figure 13 is the expected GCLF using a log-normal distribution corrected for incompleteness in magnitude,

$$dN/dM = N_0 e^{-(M-M_0)^2/2\sigma_M^2}, \tag{3}$$

where N_0 is a normalization factor, M is the absolute magnitude of the fitted bin, M_0 is the absolute magnitude of TO, and σ_M is the dispersion. The GCLF is corrected for incompleteness using the expected TO (described above) and the 3σ limit of the GCLF assuming $\sigma = 1.40 \pm 0.06$ (e.g., B. C. Whitmore et al. 1995; K. A. Alamo-Martínez et al. 2013), and for a factor

Table 4
Broadband Colors and Observational Properties of the 10 Brightest GC Candidates

Name (1)	R.A. (2)	Decl. (3)	i (4)	$(u-i)_0$ (5)	$(g-r)_0$ (6)	$(g-i)_0$ (7)	$(g-z)_0$ (8)	FWHM (9)	CLASS STAR (10)	SPREAD MODEL (11)	FLUX RADIUS (12)	M_i (13)	flag (14)
GC_SPLUS-s30s31_1	51.91487	−39.14339	19.02 ± 0.03	1.46 ± 0.14	0.48 ± 0.06	0.63 ± 0.06	0.60 ± 0.08	4.96	0.89	0.001	2.05	−12.38	02
GC_SPLUS-s26s42_2	66.72938	−34.23268	19.02 ± 0.03	⋯	1.24 ± 0.17	2.20 ± 0.17	2.54 ± 0.17	4.29	0.60	0.002	1.90	−12.38	00
GC_SPLUS-s31s38_3	64.86757	−39.47520	19.02 ± 0.02	⋯	1.20 ± 0.10	1.94 ± 0.09	2.34 ± 0.09	3.14	0.69	0.000	1.77	−12.38	00
GC_SPLUS-s25s38_4	58.42777	−32.43845	19.03 ± 0.02	2.50 ± 0.21	1.35 ± 0.09	2.24 ± 0.09	2.74 ± 0.09	6.56	0.30	0.004	2.56	−12.37	01
GC_SPLUS-s31s37_5	64.07645	−39.44286	19.03 ± 0.02	3.26 ± 0.40	1.00 ± 0.12	2.30 ± 0.11	2.85 ± 0.11	7.83	0.72	0.004	3.03	−12.37	01
GC_SPLUS-s27s32_6	50.17298	−35.15112	19.04 ± 0.03	⋯	1.16 ± 0.18	2.30 ± 0.17	2.89 ± 0.17	5.99	0.82	0.004	2.73	−12.36	00
GC_SPLUS-s29s40_7	66.96018	−37.06000	19.04 ± 0.03	2.62 ± 0.21	0.64 ± 0.05	1.04 ± 0.05	1.10 ± 0.06	3.61	0.82	0.003	1.75	−12.36	02
GC_SPLUS-s31s38_8	65.78262	−40.69203	19.05 ± 0.02	⋯	1.23 ± 0.09	2.10 ± 0.09	2.51 ± 0.09	4.22	0.88	0.009	1.82	−12.35	00
GC_SPLUS-s24s28_9	42.22746	−31.50407	19.05 ± 0.02	⋯	1.23 ± 0.10	2.08 ± 0.10	2.45 ± 0.10	2.97	0.83	0.001	1.58	−12.35	00
GC_SPLUS-s32s28_10	49.21475	−41.01128	19.05 ± 0.03	⋯	1.02 ± 0.11	1.79 ± 0.11	2.05 ± 0.11	4.04	0.67	0.001	1.90	−12.35	00

Note. (1) Assigned name, which follows the convention of FGC_field_n, where F is for Fornax and GC for globular cluster, field corresponds to the name of the pointing in which the GC candidate is located, and n is 1 for the brightest object in the i band, and increases sequentially as the magnitude increases. (2), (3) R.A., decl., in J2000. (4) Magnitude of the PSF (MAG_PSF) in the i band and magnitude error from SExtractor. (5), (8) $(u-i)_0$, $(g-r)_0$, $(g-i)_0$, and $(g-z)_0$ colors; the error is the quadrature sum of the error in each band from SExtractor. (9), (12) The structural parameters for each GC candidate: FWHM, CLASS_STAR, SPREAD_MODEL, and FLUX_RADIUS. (13) M_i magnitude. (14) FLAG classification: 00 clusters without u-band photometry; 01 determined as a reddened young cluster from u-band photometry; 02–determined as BF-GCC from u-band photometry; and 03–error in $(u-i)$ is likely to be larger than the indicated formal error.

(This table is available in its entirety in machine-readable form in the online article.)

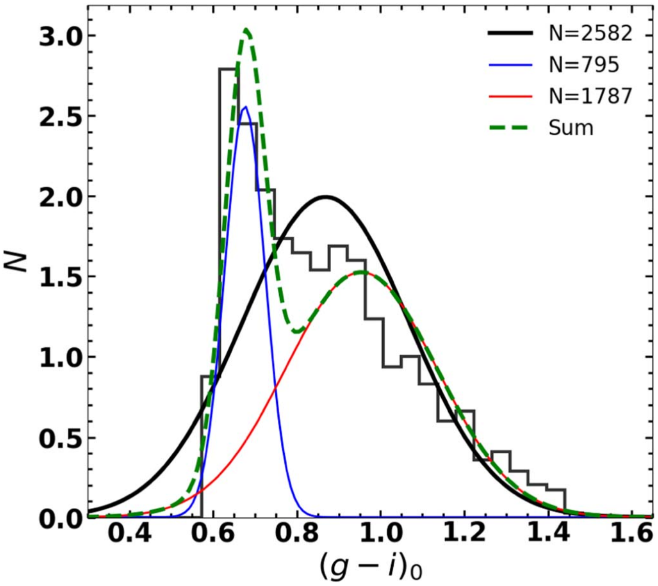

Figure 11. $g - i)_0$ color distribution for the BF-GCC sample. The black solid line is the unimodal fit returned by the GMM analysis and blue and red solid lines are the bimodal fit returned by the GMM analysis. The green dashed line is the sum of the red and blue fits.

Table 5
Total Number of GC Candidates at Differents $R_{\rm vir}$

Sample (1)	Obs (2)	Blue$_{gi}$ (3)	Red$_{gi}$ (4)	Blue$_{gz}$ (5)	Red$_{gz}$ (6)
$0.5R_{\rm vir}$	99	48	51	76	23
$1R_{\rm vir}$	315	139	176	233	82
$2R_{\rm vir}$	863	432	431	658	205
$3R_{\rm vir}$	1597	816	781	1212	385
BF-GCC	2653	1390	1263	2034	619

Note. (1) Subsamples. (2) Number of BF-GCC in each $R_{\rm vir}$. (3), (4) Number of BF-GCC in each $R_{\rm vir}$, divided by color, $(g - i)_0$. (5), (6) Number of BF-GCC in each $R_{\rm vir}$, divided by color, $(g - z)_0$.

correction caused by selection criteria in the colors, e.g., $(u - i)_0$. This factor correction was estimated by the number of nondetections in the u band (the u band is shallower) with respect to the detections in i band.

5.3. Spatial Distribution

Taking into advantage the large spatial coverage of S-PLUS, in this subsection we present the analysis of the projected spatial distribution of the identified BF-GCC, as well as that of their colors and of the GCLF at different radius from the center of Fornax.

5.3.1. GCs Spatial Distribution

In Figure 14, we show the BF-GCC (red dots) spatial distribution in RA,DEC (J2000) coordinates in the 106 FOVs ($\sim$200 deg^2) analyzed here. Different multiples (0.5, 1, 2, 3) of the virial radius, $R_{\rm vir}$ (black empty circles), centered on NGC 1399 (RA = 54.620941, DEC = −35.450657) are displayed. A compilation of spectroscopically confirmed galaxies from A. V. Smith Castelli et al. (2024; blue empty circles) and UDGs (green empty squares) from D. Zaritsky et al. (2023) are also shown.

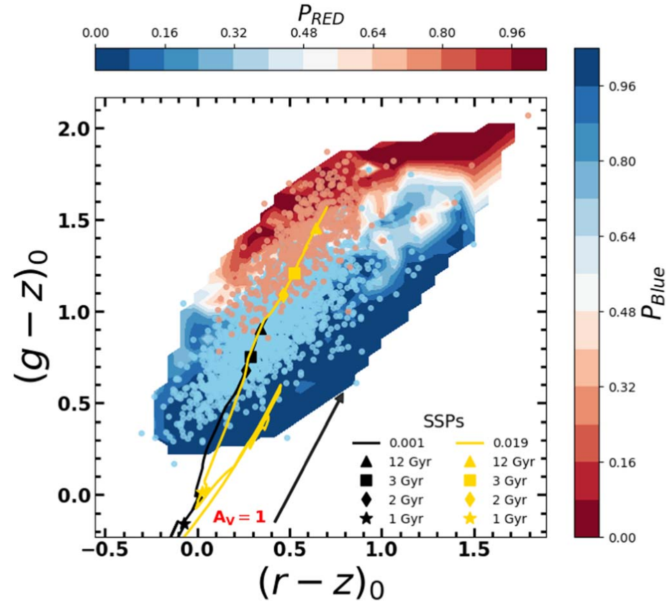

Figure 12. $(g - z)_0$ vs. $(r - z)_0$ diagram with color bars indicating the GMM probability distribution to be red (top color bar) and blue (right color bar) GC candidates. The evolutionary loci of SSPs from G. Bruzual & S. Charlot (2003) corresponding to a Kroupa IMF with $Z = 0.001$ (black solid curve) and $Z = 0.019$ (yellow solid curve) are shown. Locations corresponding to 1, 2, 3, and 12 Gyr in each locus are indicated with different symbols (see the symbol code in the plot). The reddening vector with $A_V = 1$ mag is represented by the black arrow.

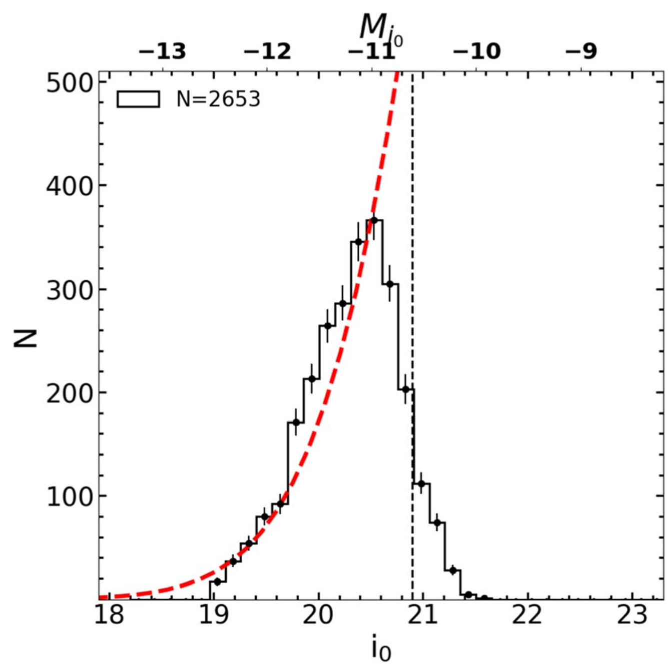

Figure 13. i-band GCLF distribution (histogram). The red dashed line is the expected GCLF using a log-normal distribution corrected for incompleteness in magnitude. The vertical dashed lines indicate the magnitude at which the detection is 50% is complete. Poisson error bars ($\sqrt{N}$) are indicated.

In Figure 14, we noted that the highest concentration of GCs is toward the center, where NGC 1399 is located. One $R_{\rm vir}$ is equivalent to $\sim$2°, which at the Fornax distance is equivalent to $\sim$720 kpc. The number of BF-GCCs inside 1 $R_{\rm vir}$ centered on NGC 1399 is 315. We note that, although all of the spectroscopically confirmed galaxies from the literature are

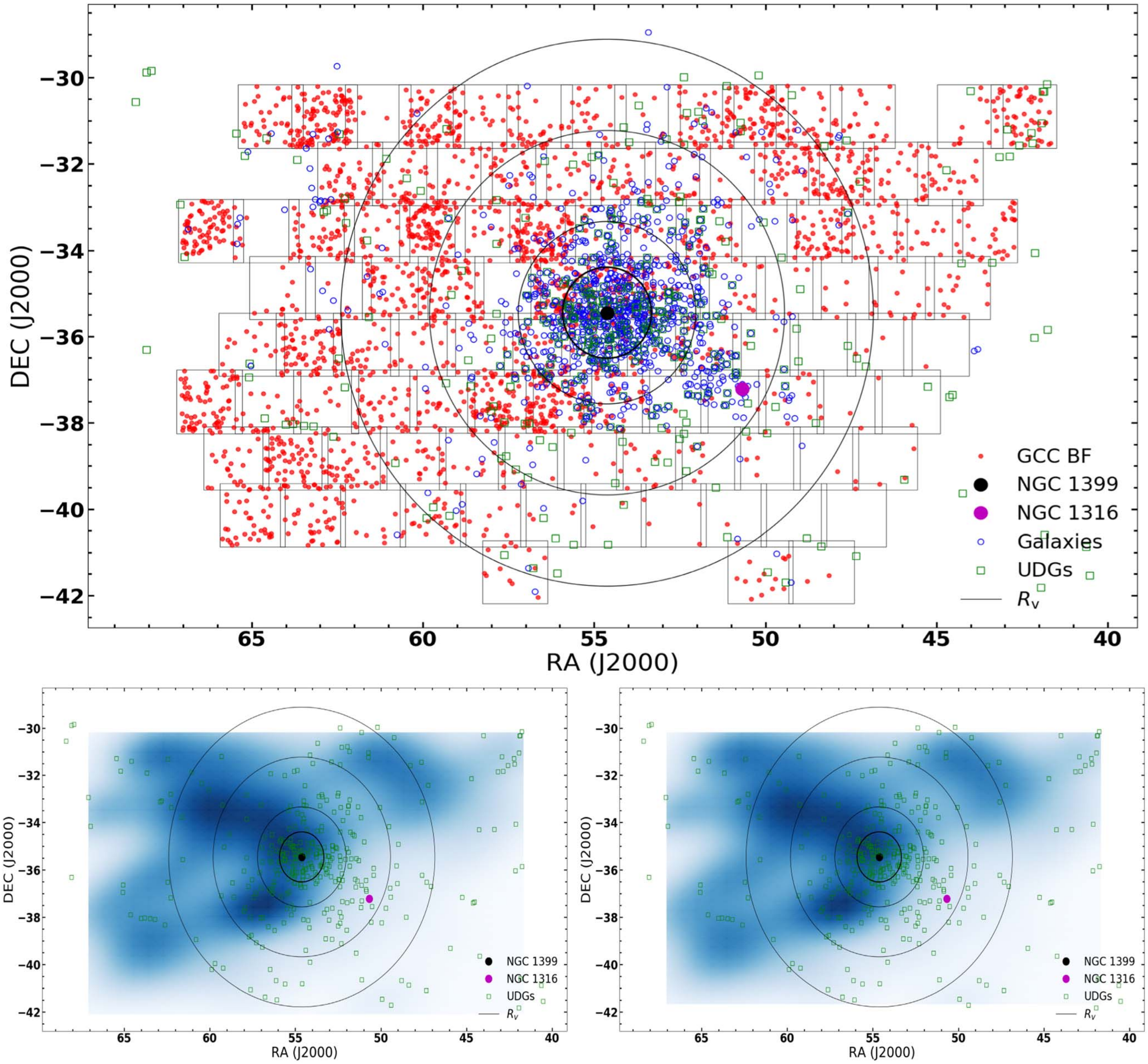

Figure 14. Spatial distribution in RA,DEC (J2000) coordinates for the BF-GCC sample (red dots). Galaxies from the literature are indicated with blue circles and green empty squares. The black empty circles are the multiples (0.5, 1, 2, 3) of the $R_{\rm vir}$ centered in NGC 1399. The black solid point represents the center of NGC 1399 galaxy. In the bottom panels, we show the GCs distribution smoothed with a Gaussian kernel (blue distribution) of the BF-GCC on the left, and including only objects identified as "PSF" by DESI on the right; see the text for more details.

shown, there are areas where a concentration of BF-GCC is displayed, lacking their host galaxies (for example, from 61°to 66° in RA and −41° to −37° in DEC). On the other hand, in the fields covering from 45°to 49° in RA and −40° to −36° in DEC, there seems to be a scarcity in the detections of GC candidates. In addition, we also note that in some FOVs, for example in s24s41 (62°to 64° and −32° to −30°), the distribution of GC candidates is homogeneous throughout the field. The difference in number of recovered BF-GCCs could be real or the result of a variation of the observing conditions. In Appendix A, we provide an analysis of different parameters such as: airmass, exposure time, and background. We find that, even if a nonlinear combination of these parameters is affecting our ability to recover GCs, it is not sufficient to explain the variation of detections. To further investigate this behavior, we calculated the reason between the different number of objects detected in a tile and the number of BF-GCCs extracted in the same tile. In fact, the observing conditions would affect in the same manner both detections. In the last row of Figure 17 in Appendix A, we show the result of this experiment, which suggests that, particularly in the southwest, the lower number of detections is probably related to observational conditions of each tile. Such a result is consistent with the maps of the sky rms and median value, which are also lower in the southwest region, reflecting worse observing conditions.

GCs literature studies in Fornax are mostly focused on the central part, where the galaxy NGC 1399 is located. For instance, L. P. Bassino et al. (2006) studied the GCs distribution in a limited central area up to a radius of 275 kpc. Another example is the study of R. D'Abrusco et al. (2016), in which all GCs are distributed within 210 kpc; whereas in M. Cantiello et al. (2018), 86% of their sample is concentrated within 0.5 $R_{\rm vir}$,

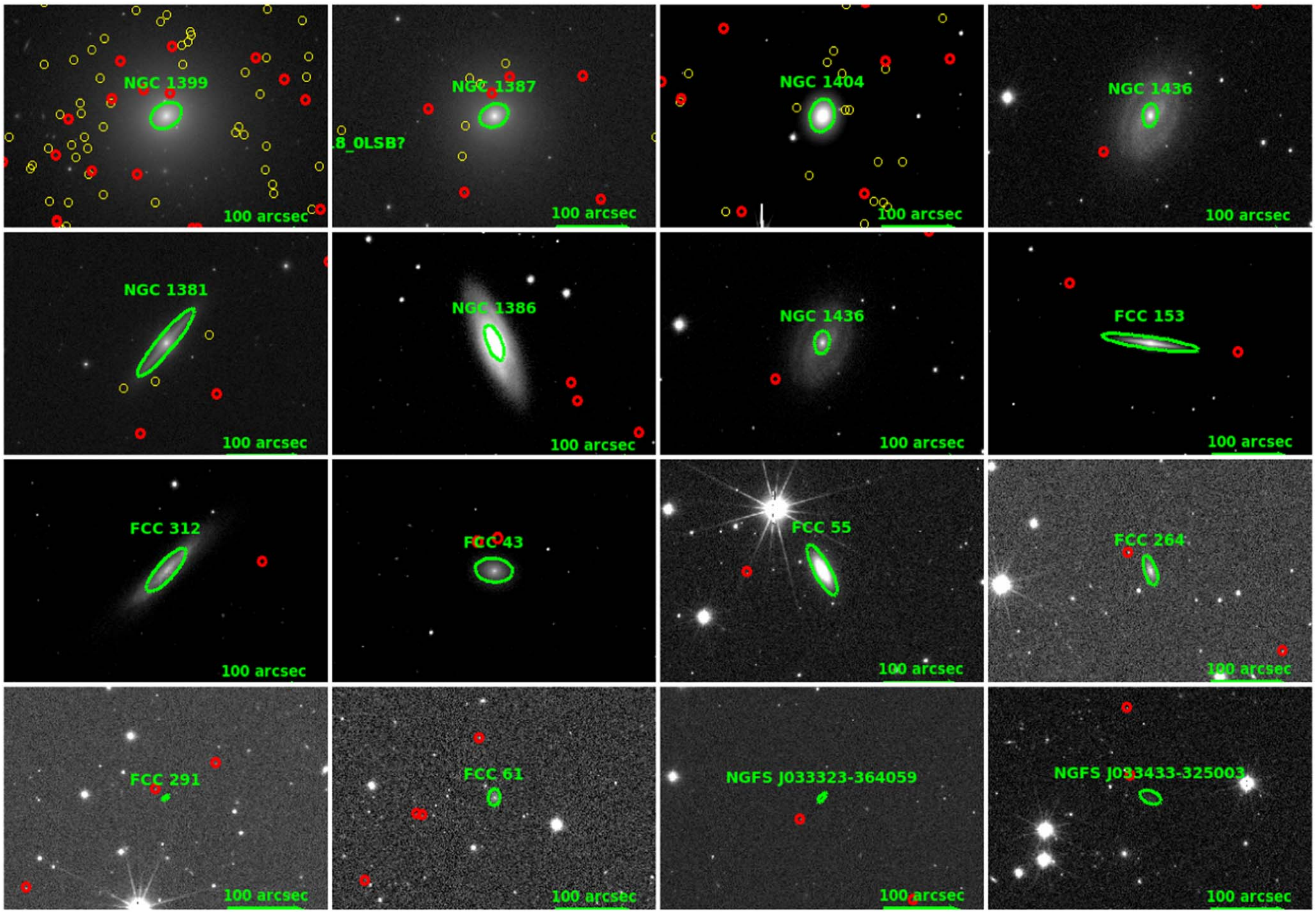

Figure 15. Sample of galaxies (green ellipses), GC candidates (red circles), and spec-GCs recovered in the S-PLUS *i* band (yellow circles). All images are snapshots in the *i* band from S-PLUS and are aligned such that north is up and east to the left, and the angular size equivalent to 100″ (green arrows) is shown.

equivalent to 360 kpc (using our distance convention). Our sample extends up to 3 $R_{\rm vir}$ with a complete spatial coverage, although it can reach up to 5 $R_{\rm vir}$ (in the east–west direction) with an incomplete spatial distribution (in the north–south direction); see Figure 14. With the spatial coverage reached in this study, we are able, for the first time, to explore the large-scale distribution of GCs within a galaxy cluster. As previously mentioned, GCs could be associated to the BCG (e.g., B. Dirsch et al. 2003; L. P. Bassino et al. 2006; J. P. Blakeslee et al. 2012), to other galaxies (e.g., D. Villegas et al. 2010; H.-S. Kim et al. 2013), or to the intracluster light (e.g., Y. Schuberth et al. 2008; S. Kaviraj et al. 2012; M. Reina-Campos et al. 2022; M. Kluge et al. 2024; T. Saifollahi et al. 2024). The GCs distribution also highlights the interactions between galaxies within a cluster (S. Federle et al. 2024). In the bottom panels of Figure 14, we show the distribution smoothed with a Gaussian kernel (blue distribution) of the BF-GCC on the left, and on the right the same distribution including only objects identified as "PSF" by DESI (see Section 4.5), therefore leaving only objects consistent with a PSF-like profile to have even a higher purity. The bottom-left and -right panels of Figure 14 present similar features: with the clustering of GCs toward northeast and a lower density of GCs (caused by worse observing conditions; see Figure 17) toward the southwest. In the northeastern area, the darkest smoothed areas, which correspond to the highest density of GCs distribution, share the same spatial distribution as UDGs. Previous studies in Virgo (e.g., M. Powalka et al. 2018) and Fornax (e.g., R. D'Abrusco et al. 2022) have observed substructures in the GC population around large galaxies. The substructures are expected in galaxy formation scenarios that involve accretion or merger events. Here we note that the GCs might be clustered along substructures, which might trace back to the cluster build up, in both panels, with the right panel only presenting a lower number of objects.

As illustrated in Figure 15, we show snapshots of 20 galaxies with different Hubble morphological types (E, S, S0, and dwarfs). Each stamp shows the detected GC candidates (red circles) and spec-GCs recovered in S-PLUS *i*-band (yellow circles) close to each galaxy. The green ellipses plotted are the semiaxes A_IMAGE and B_IMAGE multiplied by the KRON_RADIUS obtained in our photometry analysis. Each image has a dimension of 390″ × 318″. In the literature, there are ∼1000 spectroscopically confirmed galaxies belonging to the Fornax, most of which are also located in the inner parts of the cluster. A large portion of GC candidates is located in the outer parts of Fornax, where there are no classified galaxies yet. Thus, with our GC candidates sample, it is possible to detect galaxies with an indirect method, increasing the number of galaxies classified in Fornax and also studying disrupted field GCs that do not have a host galaxy. In the next subsections, we further discuss the GC candidates' spatial distribution.

5.3.2. *Colors and GCLF at Different* R_{vir}

In various studies, it has been found that the spatial distribution of GCs is bimodal (e.g., S. E. Zepf &

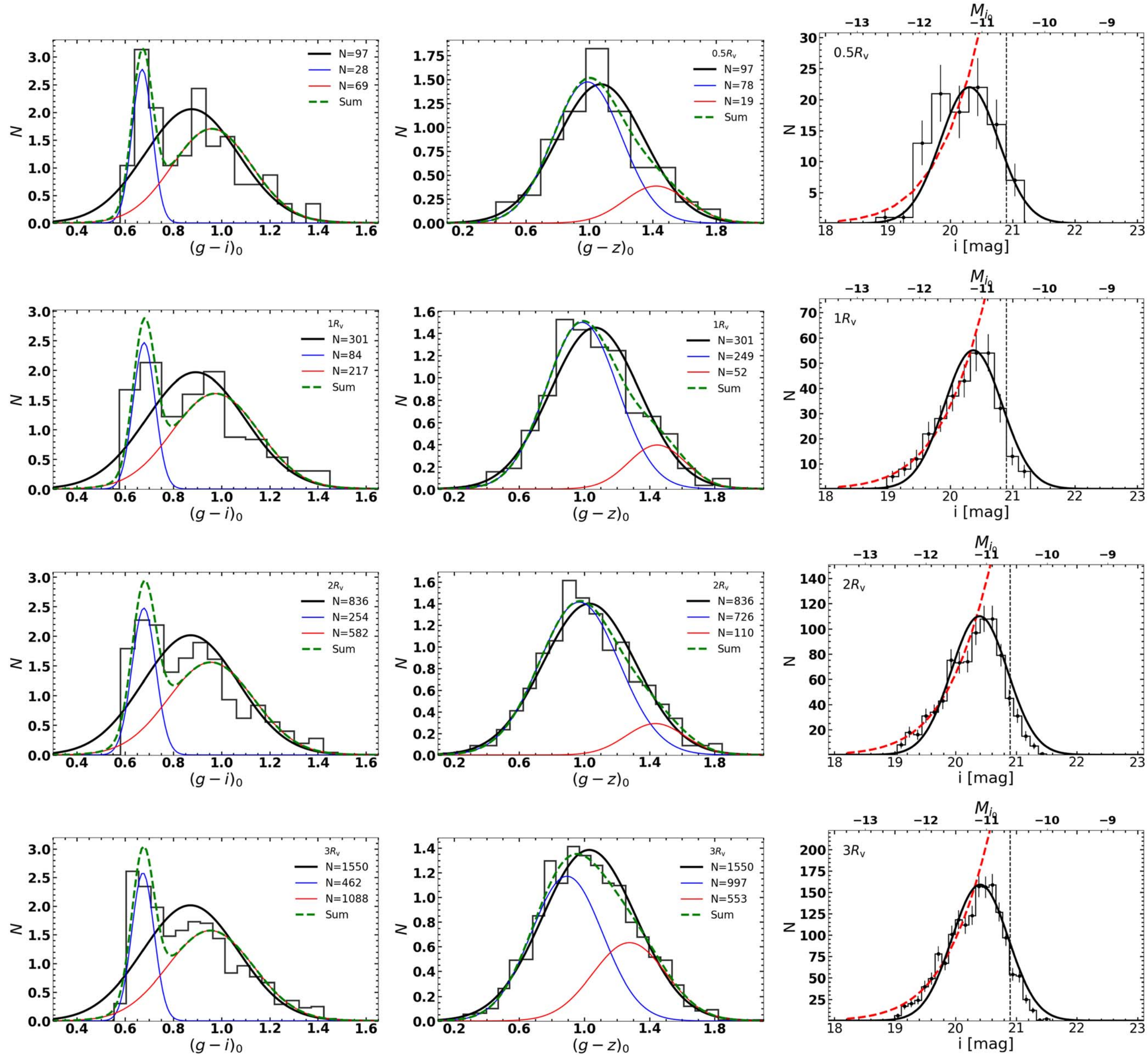

Figure 16. Colors and GCLF at different $R_{\rm vir}$ 0.5, 1, 2, and 3 (from the top to bottom panels). The first and second columns are the $(g-i)_0$ and $(g-z)_0$ colors; the color code is the same as in Figure 11. The third column shows the i-GCLF; the color code is the same as in Figure 13.

K. M. Ashman 1993), in which the most metal-poor clusters are distributed in the outer parts of their parent galaxies, while the metal-rich ones present a more homogeneous distribution with a concentration peak toward the inner parts of the host galaxies (e.g., J. R. Hargis & K. L. Rhode 2014; S. S. Kartha et al. 2014). In this scenario, a color gradient is likely, with the redder GCs concentrated toward the center, and the bluer GCs populating the outermost parts of the system (J. R. Hargis & K. L. Rhode 2014). With S-PLUS data, it is possible to expand this gradient to a large number of colors at radii of up to 5 $R_{\rm vir}$ in RA.

In the first and second columns of Figure 16, we show the $(g-i)_0$ and $(g-z)_0$ color distributions at differents $R_{\rm vir}$ (0.5, 1, 2, and 3). Near NGC 1399 (i.e., the Fornax center), a possible trace of bimodality in the color $(g-i)_0$ can be seen. As we move away from the cluster center, this bimodality fades and becomes a long tail of red clusters. On the contrary, in $(g-z)_0$ color, a bimodality distribution is preserved at large distances from the center, similarly to the observations in the Virgo cluster (e.g., P. R. Durrell et al. 2014; H.-X. Zhang et al. 2015). In both colors, it can be observed that the GC candidates with a bluer color are predominant with respect to the GC candidates with redder colors. A larger population of blue GC candidates may be due to the existence of dwarf galaxies (not yet cataloged), which host bluer GCs populations due to their low mass (mass–metallicity ratio, P. Côté et al. 1998). According to the fitting results from GMM (Table 7 in Appendix B) in each subsample, we concluded that the bimodality in both colors is preserved as we move away from the center.

In the third column of Figure 16, we show the GCLF distribution in the i band at different $R_{\rm vir}$ (0.5, 1, 2, and 3). We obtained the peak magnitude from the fit of the GCLF made with GMM, using a single Gaussian (black solid line). The GCLF corrected for incompleteness is the red dashed line. It is noted that the mean value found with GMM of each distribution observed increases slightly at differents $R_{\rm vir}$ (20.21 $\pm$ 0.05, 20.27 $\pm$ 0.03, 20.29 $\pm$ 0.02, and 20.31 $\pm$ 0.01), which implies a mass decrease of $\sim$10% between the central and the outermost peak distribution, assuming the proportionality between mass to light. The increase in the peak mass of the GCLF should be related to the concentration of massive galaxies, toward the center (A. Jordán et al. 2007b); the mean GCs mass is greater in massive galaxies compared to less-massive ones (e.g., W. E. Harris et al. 2013; R. A. González-Lópezlira et al. 2022), while the decrease in mass is related to the concentration of dwarf galaxies toward the outer parts of the cluster. However, this result must be taken with care, because we are not looking at individual galaxies, and the differences in the estimated mass are within the errors (2σ).

5.4. Missing Galaxies

The number of galaxies spectroscopically confirmed or considered likely members on morphological basis in Fornax is $\sim$1000 (see A. V. Smith Castelli et al. 2024). On the other hand, reviewing the literature (e.g., A. Jordán et al. 2007a; D. Villegas et al. 2010; R. D'Abrusco et al. 2022; T. Saifollahi et al. 2024), and rejecting repeated galaxies, there are 75 galaxies in Fornax in which $\sim$10,000 GCs have been observed. If we assume that the BF-GCC sample extracted in this work is also associated to galaxies, the total number of GCs associated to the Fornax cluster is $\sim$13,000. If, in a first-order approximation, we assume that all galaxies have the same number of GCs and that the number of GCs in the Fornax cluster should be similar for the rest of the 925 galaxies, the total number of GCs would be $\sim$173,000 ($N_TOT = N_{\rm GAL,SPEC}/N_{\rm GAL,OBS} \times N_{\rm GC,OBS}$), of the same order of magnitude of GCs associated to the Abell 1689 (K. A. Alamo--Martínez et al. 2013) cluster. Yet, the number of GCs observed in a galaxy depends on the galaxy mass and morphology, with irregular and dwarf galaxies having numbers from zero to tens (e.g., F. Annibali et al. 2018; D. J. Prole et al. 2019; N. Karim et al. 2024), while galaxies similar in mass to the MW have around tens to hundreds (e.g., W. E. Harris 1996, 2010, $\sim$160) GCs, and for massive early-type galaxies, this is of the order of hundreds to thousands (e.g., W. E. Harris et al. 2014). According with D. Villegas et al. (2010), the galaxy (FCC_335) has the minimum number (14 or 7, taking into account contaminants) of GCs, and the results obtained from simulations usually assign a number of $\sim$10 GCs to low- or intermediate-mass galaxies (e.g., M. Reina-Campos et al. 2022). Considering that the Fornax cluster has a large population of dwarf galaxies, it is possible to make two statements for the BF-GCC sample: (a) a large percentage of GCs are not really bound to galaxies and belong to the intracluster medium; indeed T. Saifollahi et al. (2024) found that a percent of the Fornax GCs are associated to the intracluster medium; and (b) the number of galaxies belonging to Fornax is greatly underestimated outside 1 $R_{\rm vir}$; as explained in Section 5.3.1, the GC distribution can be used to identify the locations of galaxies belonging to the Fornax cluster and trace back the process of clustering, where the passages of newly acquired members within the cluster potential, or galaxy–galaxy interactions, may leave behind a tale of stripped GCs. Further work, using S-PLUS photometric data (e.g., R. F. Haack et al. 2025, in preparation) is currently underway with the purpose of identifying new galaxy candidates. In addition, spectroscopic confirmation using data from the Gemini South telescope for a sample of GCs and missing galaxies is currently ongoing (e.g., L. Lomelì-Núñez et al. 2025, in preparation). Finally, the CHANCES/4MOST survey (C. Sifón et al. 2024), which will recover the spectroscopic redshift of galaxies in galaxies clusters out to 5 effective radii (including the Fornax cluster), will be a breakthrough in our understanding of cluster formation, and solve the issue of missing galaxies ($m_r < 20.5$).

6. Conclusions

We studied the GC system in Fornax over $\sim$200 square degrees, using homogeneous data taken through the 12 optical bands of S-PLUS. We used SExtractor plus PSFEx to perform PSF photometry and developed a method of selection of GCs, using structural, evolutionary, and distance (GAIA and SED fitting template) parameters. Detection of simulated clusters was carried out to obtain the incompleteness as a function of magnitude. We used u-band photometry to evaluate the contamination of our sample of GC candidates by stars, background galaxies, or YSCs reddened. The contaminating fraction was found to be $\sim$20%. In a follow-up paper, the GC systems associated to individual galaxies will be studied; we additionally are obtaining spectroscopic data for a subsample of objects to obtain spectroscopic confirmation of their association to the Fornax cluster.

We used our data set to construct 10 and 15 colors in broad and narrow bands, respectively. We performed statistical tests to evaluate the bimodality of colors, finding that globally, according to GMM results and visual inspection, there is evidence of color bimodality in two colors, namely, $(g-i)_0$ and $(g-z)_0$ in the broad bands. On the contrary, in the narrow bands, we did not find strong statistical evidence to confirm bimodality in any color. A possible explanation for not finding bimodality in the narrowband colors may be related to the nature itself of the narrowband filters, since they only sample a small spectral range. At the same time, the larger error on the magnitude estimations in the narrow bands might extend the color distribution, fading the bimodality. Also, we studied the $(g-i)_0$ and $(g-z)_0$ color distributions at differents virial radii (0.5, 1, 2, and 3). We found that near the Fornax center, there is a clear trace of bimodality in the color $(g-i)_0$. As we move away from the center of the cluster, the bimodality fades and becomes a long tail of red clusters. Dissimilarly, in the $(g-z)_0$ color, a bimodality distribution is preserved at large distances from the center.

We construct the GCLF in the 12 bands highlighting two points: (a) in all bands, the log-normal distribution typical for GC systems can be estimated, and it is found to increase smoothly up to reaching a peak value, and then again to decrease smoothly. However, (b) with the S-PLUS i-band 50% completeness magnitude of 21.44, we are unable to reach the TO generally observed in early-type galaxies. Thus, we are only sampling the bright end of the GCLF. Also, we studied the GCLF at differents virial radii (0.5, 1, 2, and 3), and it is noted that the peak of each distribution observed increases slightly at different values of $R_{\rm vir}$, which implies a mass increment assuming the proportionality between mass and light, maybe resulting from the infall of group and filaments into the cluster.

Acknowledgments

L.L.N. thanks Fundação de Amparo à Pesquisa do Estado do Rio de Janeiro (FAPERJ) for granting the postdoctoral research fellowship E-40/2021(280692). A.C. acknowledges Fundação de Amparo à Pesquisa do Estado do Rio de Janeiro (FAPERJ) for granting the research fellowship "Apoio a jovem pesquisador fluminense" E-40/2021(270993) and the CNPQ fellowship "Produtividade em Pesquisa do CNPq - Nível 2." A.V.S.C. acknowledges financial support from CONICET (PIP 1504), Agencia I+D+i (PICT 2019-03299), and Universidad Nacional de La Plata (Argentina). S.W. is supported by the United Kingdom Research and Innovation (UKRI) Future Leaders Fellowship "Using Cosmic Beasts to uncover the Nature of Dark Matter" (grant No. MR/X006069/1). P.K.H. gratefully acknowledges the Fundação de Amparo à Pesquisa do Estado de São Paulo (FAPESP) for the support grant 2023/14272-4. A.A.C. acknowledges financial support from the Severo Ochoa grant CEX2021-001131-S funded by MCIN/AEI/10.13039/501100011033. C.L.-D. acknowledges financial support from the ESO Comite Mixto 2022. S.P. acknowledges CNPq Fellow, Gemini Science Fellow. T.S.G. would like to thank CNPq (PQ grant 314449/2023-0) and FAPERJ (JCNE grant 201.309/2021). M.G. acknowledges support from FAPERJ grant E-26/211.370/2021. K.M.D. thanks the support of the Serrapilheira Institute (grant Serra-1709-17357) as well as that of the Brazilian National Research Council (CNPq grant 308584/2022-8) and of the Rio de Janeiro Research Foundation (FAPERJ grant E-32/200.952/2022), Brazil. V.F. thanks Fundação Coordenação de Aperfeiçoamento de Pessoal de Nìvel Superior (CAPES) for granting the postdoctoral research fellowship Programa de Desenvolvimento da Pós-Graduação (PDPG)-Pós Doutorado Estratégico, Edital n°16/2022 and the Finance Code 001 (88887.838401/2023-00) funding.

The S-PLUS project, including the T80S robotic telescope and the S-PLUS scientific survey, was founded as a partnership between the Sao Paulo Research Foundation (FAPESP), the Observatório Nacional (ON), the Federal University of Sergipe (UFS), and the Federal University of Santa Catarina (UFSC), with important financial and practical contributions from other collaborating institutes in Brazil, Chile (Universidad de La Serena), and Spain (Centro de Estudios de Fisica del Cosmos de Aragon, CEFCA).

This research has made use of the NASA/IPAC Extragalactic Database (NED), which is operated by the California Institute of Technology, under contract with the National Aeronautics and Space Administration.

This work has made use of data from the European Space Agency (ESA) mission Gaia (https://www.cosmos.esa.int/gaia), processed by the Gaia Data Processing and Analysis Consortium (DPAC, https://www.cosmos.esa.int/web/gaia/dpac/consortium). Funding for the DPAC has been provided by national institutions, in particular the institutions participating in the Gaia Multilateral Agreement.

The DESI Legacy Imaging Surveys consist of three individual and complementary projects: the Dark Energy Camera Legacy Survey (DECaLS), the Beijing-Arizona Sky Survey (BASS), and the Mayall z-band Legacy Survey (MzLS). DECaLS, BASS, and MzLS together include data obtained, respectively, at the Blanco telescope, Cerro Tololo Inter-American Observatory, NSF's NOIRLab; the Bok telescope, Steward Observatory, University of Arizona; and the Mayall telescope, Kitt Peak National Observatory, NOIRLab. NOIRLab is operated by the Association of Universities for Research in Astronomy (AURA) under a cooperative agreement with the National Science Foundation. Pipeline processing and analyses of the data were supported by NOIRLab and the Lawrence Berkeley National Laboratory (LBNL). Legacy Surveys also uses data products from the Near-Earth Object Wide-field Infrared Survey Explorer (NEOWISE), a project of the Jet Propulsion Laboratory/California Institute of Technology, funded by the National Aeronautics and Space Administration. Legacy Surveys was supported by: the Director, Office of Science, Office of High Energy Physics of the U.S. Department of Energy; the National Energy Research Scientific Computing Center, a DOE Office of Science User Facility; the U.S. National Science Foundation, Division of Astronomical Sciences; the National Astronomical Observatories of China, the Chinese Academy of Sciences and the Chinese National Natural Science Foundation. LBNL is managed by the Regents of the University of California under contract to the U.S. Department of Energy. The complete acknowledgments can be found at https://www.legacysurvey.org/acknowledgment/.

Data availability

This paper is based on publicly available archival data. The complete version of Table 4 is included as a machine-readable table. All of the fits files are stored in the S-PLUS cloud (https://splus.cloud).

Facility: S-PLUS.

Software: Source-Extractor (E. Bertin & S. Arnouts 1996), PSFEx (E. Bertin 2011), GALAXEV (G. Bruzual & S. Charlot 2003), GMM (A. L. Muratov & O. Y. Gnedin 2010), IRAF (D. Tody 1986).

Appendix A
Image Features

All astronomical observations are subject to weather. The conditions imposed by these two major factors directly influence the image quality and the final detection and measurements that we can achieve. In Figure 17, we show four examples of the parameters that predetermine the final results, named: AIRMASS, SATUR_LEVEL, and the MEDIAN and RMS of the background. In the left panels of Figure 17, the parameters are plotted versus the total number (N_{Total}) of sources detected in each FOV. In the right panels of Figure 17, the parameters are color coded in (RA,DEC) space. In the case of a higher value of AIRMASS reported, a lower number objects is recovered, while for SATUR_LEVEL, the trend is inversed: for a higher value of saturation, a greater number objects is recovered. In the cases of MEDIAN and RMS, a bimodal distribution appears, where the trend is not clear. However, in the bottom panel, it is observed that panels with the lower values of MEDIAN and RMS are in the southwest region. It is in these FOVs where our selection of GC candidates is smaller in proportion to the rest of the pointings. In the saturation color space, however, it is observed that in the same region (southwest), the values are highest in comparison with the rest of the FOVs. After this brief analysis, it is possible to conclude that the parameters that determine the detection and selection of GC candidates have a nonlinear relationship between them.

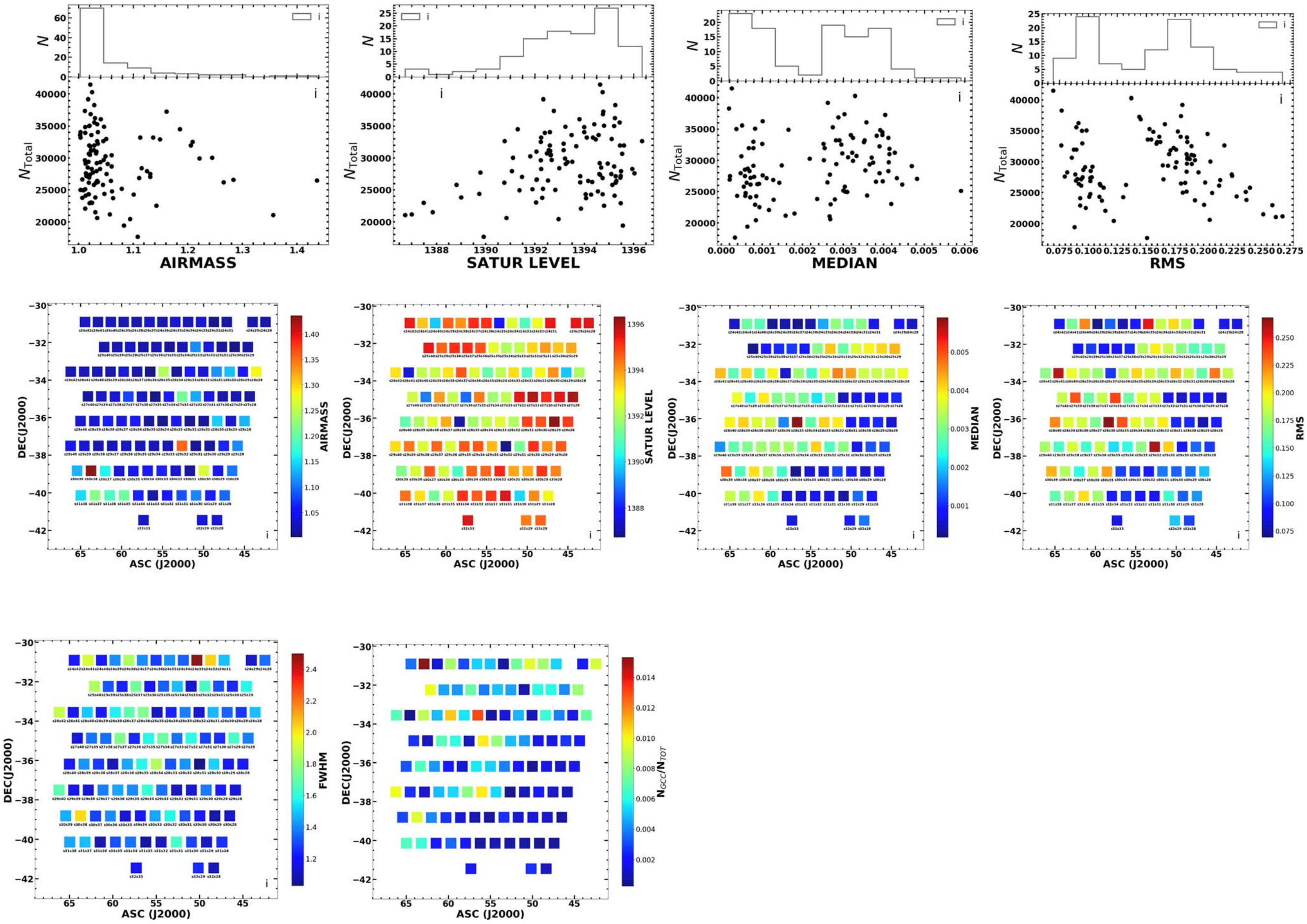

Figure 17. Observational properties in the 106 FOVs in the i band. In the first row of panels, we show the parameters: AIRMASS, SATUR_LEVEL, MEDIAN, and RMS vs. the total number of sources detected in each FOV. In the second row of panels, we show all of the FOVs in (RA,DEC) space with a color coded for each parameter: AIRMASS, SATUR_LEVEL, MEDIAN RMS. The third row of panels shows the FWHM and ratio of the GCC divided by the total sources detected in each field.

Appendix B
Statistical Colors Results

We used Gaussian mixture modeling (GMM) code (A. L. Muratov & O. Y. Gnedin 2010) to confirm the presence of bimodality in the color distributions according to the analysis presented in Section 5.1. In Tables 6 and 7, we present the GMM statistics results for Figure 11 and the left and central panels of Figure 16, respectively.

Table 6
GMM Fitting Values for Colors Distribution

Unimodal Results			Bimodal Results											
Color (1)	Peak (2)	σ (3)	Peak1 (4)	Peak2 (5)	$\sigma1$ (6)	$\sigma2$ (7)	$N_{\rm GC}^{\rm TOT}$ (8)	f_2 (9)	D (10)	Kurtosis (11)	p-values (12)			Bi (13)
Width Bands														
$(u-g)_0$	0.74 ± 0.01	0.30 ± 0.01	0.59 ± 0.03	0.9 ± 0.03	0.2 ± 0.01	0.3 ± 0.01	2582	0.47	1.21 ± 0.08	0.47	0.01	0.6	1.00	N
$(u-r)_0$	1.32 ± 0.01	0.37 ± 0.01	1.26 ± 0.02	1.46 ± 0.24	0.32 ± 0.02	0.43 ± 0.09	2582	0.31	0.53 ± 0.82	0.38	0.01	0.81	1.00	N
$(u-i)_0$	1.60 ± 0.01	0.38 ± 0.01	1.47 ± 0.04	1.88 ± 0.14	0.29 ± 0.02	0.39 ± 0.05	2582	0.32	1.19 ± 0.48	0.30	0.01	0.82	0.99	N
$(u-z)_0$	1.76 ± 0.01	0.41 ± 0.01	1.62 ± 0.04	2.04 ± 0.12	0.32 ± 0.02	0.42 ± 0.03	2582	0.33	1.14 ± 0.35	0.20	0.01	0.24	0.99	N
$(g-r)_0$	0.59 ± 0.01	0.19 ± 0.01	0.52 ± 0.24	0.6 ± 0.07	0.09 ± 0.06	0.20 ± 0.05	2582	0.87	0.48 ± 1.58	0.29	0.01	0.64	0.99	N
$(g-i)_0$	0.87 ± 0.01	0.2 ± 0.01	0.68 ± 0.01	0.95 ± 0.01	0.05 ± 0.01	0.18 ± 0.01	2582	0.69	2.10 ± 0.04	-0.31	0.01	0.23	0.01	Y
$(g-z)_0$	1.02 ± 0.01	0.29 ± 0.01	0.92 ± 0.03	1.35 ± 0.08	0.22 ± 0.01	0.20 ± 0.03	2582	0.24	2.02 ± 0.28	-0.28	0.01	0.09	0.01	Y
$(r-i)_0$	0.28 ± 0.01	0.15 ± 0.01	0.27 ± 0.0	0.37 ± 0.1	0.13 ± 0.01	0.24 ± 0.03	2582	0.11	0.51 ± 0.8	1.47	0.01	0.63	1.00	N
$(r-z)_0$	0.43 ± 0.01	0.23 ± 0.01	0.42 ± 0.01	0.88 ± 0.2	0.21 ± 0.01	0.35 ± 0.07	2582	0.02	1.60 ± 1.08	1.19	0.01	0.11	1.00	N
$(i-z)_0$	0.15 ± 0.01	0.18 ± 0.01	0.14 ± 0.01	0.17 ± 0.05	0.15 ± 0.02	0.23 ± 0.02	2582	0.37	0.17 ± 0.4	0.62	0.01	0.82	1.00	N
Narrow Bands														
$(\rm J0378-J0410)_0$	0.27 ± 0.02	0.49 ± 0.02	0.26 ± 0.04	0.33 ± 0.13	0.40 ± 0.08	0.82 ± 0.18	772	0.15	0.11 ± 0.16	1.95	0.01	0.93	1.00	N
$(\rm J0378-J0430)_0$	0.30 ± 0.02	0.49 ± 0.01	0.29 ± 0.12	2.14 ± 0.74	0.47 ± 0.05	0.12 ± 0.19	565	0.01	5.37 ± 2.04	0.52	0.01	0.01	1.00	N
$(\rm J0378-J0515)_0$	0.69 ± 0.02	0.47 ± 0.01	0.62 ± 0.34	0.74 ± 0.57	0.55 ± 0.12	0.38 ± 0.19	748	0.54	0.25 ± 1.81	0.47	0.15	0.86	1.00	N
$(\rm J0378-J0660)_0$	1.11 ± 0.02	0.49 ± 0.01	1.10 ± 0.43	1.19 ± 0.53	0.46 ± 0.21	0.88 ± 0.29	771	0.05	0.12 ± 1.73	0.72	0.02	0.93	1.00	N
$(\rm J0378-J0861)_0$	1.41 ± 0.02	0.54 ± 0.02	1.41 ± 0.55	1.41 ± 0.50	0.28 ± 0.24	0.58 ± 0.20	762	0.83	0.01 ± 1.75	0.45	0.23	1.00	0.99	N
$(\rm J0410-J0430)_0$	0.06 ± 0.02	0.46 ± 0.02	0.07 ± 0.05	0.04 ± 0.22	0.36 ± 0.09	0.73 ± 0.18	565	0.22	0.05 ± 0.57	1.75	0.01	0.98	1.00	N
$(\rm J0410-J0515)_0$	0.41 ± 0.02	0.48 ± 0.02	0.27 ± 0.33	0.45 ± 0.05	0.70 ± 0.15	0.38 ± 0.06	748	0.79	0.32 ± 0.92	1.35	0.01	0.83	1.00	N
$(\rm J0410-J0660)_0$	0.84 ± 0.02	0.51 ± 0.02	0.77 ± 0.27	0.85 ± 0.03	0.75 ± 0.20	0.42 ± 0.13	771	0.79	0.13 ± 0.72	0.99	0.01	0.92	1.00	N
$(\rm J0410-J0861)_0$	1.14 ± 0.02	0.56 ± 0.01	0.01 ± 0.51	1.16 ± 0.19	0.22 ± 0.12	0.54 ± 0.08	762	0.98	2.76 ± 1.24	0.01	0.77	0.17	0.60	N
$(\rm J0430-J0515)_0$	0.42 ± 0.02	0.46 ± 0.02	0.23 ± 0.71	0.42 ± 0.08	1.07 ± 0.39	0.40 ± 0.16	559	0.95	0.25 ± 2.02	4.15	0.01	0.88	1.00	N
$(\rm J0430-J0660)_0$	0.84 ± 0.02	0.48 ± 0.02	0.84 ± 0.47	0.84 ± 0.05	0.77 ± 0.37	0.37 ± 0.22	566	0.80	0.01 ± 1.32	2.85	0.01	1.00	1.00	N
$(\rm J0430-J0861)_0$	1.14 ± 0.02	0.55 ± 0.02	0.91 ± 1.00	1.14 ± 0.38	1.36 ± 0.49	0.52 ± 0.16	559	0.98	0.22 ± 2.67	1.87	0.01	0.88	1.00	N
$(\rm J0515-J0660)_0$	0.43 ± 0.01	0.28 ± 0.01	0.40 ± 0.02	0.51 ± 0.07	0.21 ± 0.03	0.40 ± 0.06	749	0.29	0.36 ± 0.25	1.48	0.01	0.82	1.00	N
$(\rm J0515-J0861)_0$	0.73 ± 0.01	0.37 ± 0.01	0.67 ± 0.07	1.06 ± 0.47	0.33 ± 0.08	0.43 ± 0.11	740	0.14	1.02 ± 1.60	0.46	0.01	0.60	0.99	N
$(\rm J0660-J0861)_0$	0.30 ± 0.01	0.24 ± 0.01	0.29 ± 0.13	1.53 ± 0.53	0.23 ± 0.05	0.06 ± 0.15	763	0.01	7.47 ± 3.21	1.81	0.01	0.01	1.00	N

Note. (1) Color. (2)–(3) Mean and standard deviation of the first peak in the double-Gaussian model. (4)–(5) Mean and sigma of the second peak in the double-Gaussian model. (6) Total number of GCs. (7) Fraction of $N_{\rm GC}^{\rm TOT}$ associated with the second peak. (8) Separation of the means relative to their widths. (9) GMM p-values based on the likelihood-ratio test $p(\chi^2)$, peak separation p(DD), and Kurtosis p(kurt) (lower p-values are more significant). (10) Kurtosis of the colors distribution. (11) Bimodality final evaluation: Y (confirmation), N (discard).

Table 7
GMM Fitting Values for Color Distributions at Differents $R_{\rm vir}$

Unimodal Results			Bimodal Results											
Color (1)	Peak (2)	σ (3)	Peak1 (4)	Peak2 (5)	$\sigma 1$ (6)	$\sigma 2$ (7)	$N_{\rm GC}^{\rm TOT}$ (8)	f_2 (9)	D (10)	Kurtosis (11)	p-values (12)			Bi (13)
0.5 $R_{\rm vir}$														
$(g-i)_0$	0.88 ± 0.02	0.19 ± 0.01	0.67 ± 0.06	0.96 ± 0.10	0.04 ± 0.04	0.17 ± 0.03	97	0.71	2.38 ± 0.50	−0.60	0.01	0.44	0.11	Y
$(g-z)_0$	1.07 ± 0.03	0.28 ± 0.02	0.99 ± 0.11	1.42 ± 0.19	0.22 ± 0.05	0.20 ± 0.08	97	0.19	2.07 ± 1.08	−0.07	0.71	0.56	0.63	Y
1 $R_{\rm vir}$														
$(g-i)_0$	0.89 ± 0.01	0.20 ± 0.01	0.68 ± 0.05	0.98 ± 0.09	0.04 ± 0.03	0.18 ± 0.03	301	0.72	2.26 ± 0.37	−0.42	0.01	0.31	0.06	Y
$(g-z)_0$	1.07 ± 0.02	0.28 ± 0.01	0.99 ± 0.04	1.45 ± 0.13	0.22 ± 0.03	0.18 ± 0.05	301	0.17	2.32 ± 0.59	−0.21	0.09	0.30	0.27	Y
2 $R_{\rm vir}$														
$(g-i)_0$	0.87 ± 0.01	0.20 ± 0.01	0.68 ± 0.01	0.96 ± 0.01	0.05 ± 0.01	0.18 ± 0.01	836	0.70	2.13 ± 0.08	−0.27	0.01	0.20	0.06	Y
$(g-z)_0$	1.03 ± 0.01	0.28 ± 0.01	0.97 ± 0.03	1.44 ± 0.11	0.24 ± 0.02	0.18 ± 0.04	836	0.13	2.17 ± 0.44	−0.11	0.03	0.17	0.30	Y
3 $R_{\rm vir}$														
$(g-i)_0$	0.87 ± 0.01	0.20 ± 0.01	0.67 ± 0.01	0.95 ± 0.01	0.05 ± 0.01	0.18 ± 0.01	1550	0.70	2.15 ± 0.05	−0.34	0.01	0.17	0.01	Y
$(g-z)_0$	1.03 ± 0.01	0.29 ± 0.01	0.89 ± 0.05	1.28 ± 0.10	0.22 ± 0.03	0.22 ± 0.03	1550	0.36	1.73 ± 0.30	−0.24	0.01	0.21	0.01	Y

Note. Same code as in Table 6.

Appendix C
Transformation to Johnson–Cousin System

The majority of the photometric data for GCs in the MW and external galaxies is reported in the standard Johnson–Cousins *UBVRI* system (M. S. Bessell 1990). Hence, in order to compare the results obtained from our study to that obtained in other galaxies, it is necessary to transform our *u, g, r, i*, and *z* magnitudes and colors into the standard system. The corresponding transformation equations are discussed in detail by K. Jordi et al. (2006). The transformation between *ugriz* and Johnson–Cousins systems is given by the equations:

$$u - g = (0.750 \pm 0.050) \times (U - B) + (0.770 \pm 0.070) \times (B - V) + (0.720 \pm 0.040) \tag{C1}$$

$$g - V = (0.596 \pm 0.009) \times (B - V) - (0.148 \pm 0.007) \tag{C2}$$

$$g - B = (-0.401 \pm 0.009) \times (B - V) - (0.145 \pm 0.006). \tag{C3}$$

Appendix D
GCLFs

For completeness, we show the 12-band GCLFs in Figure 18.

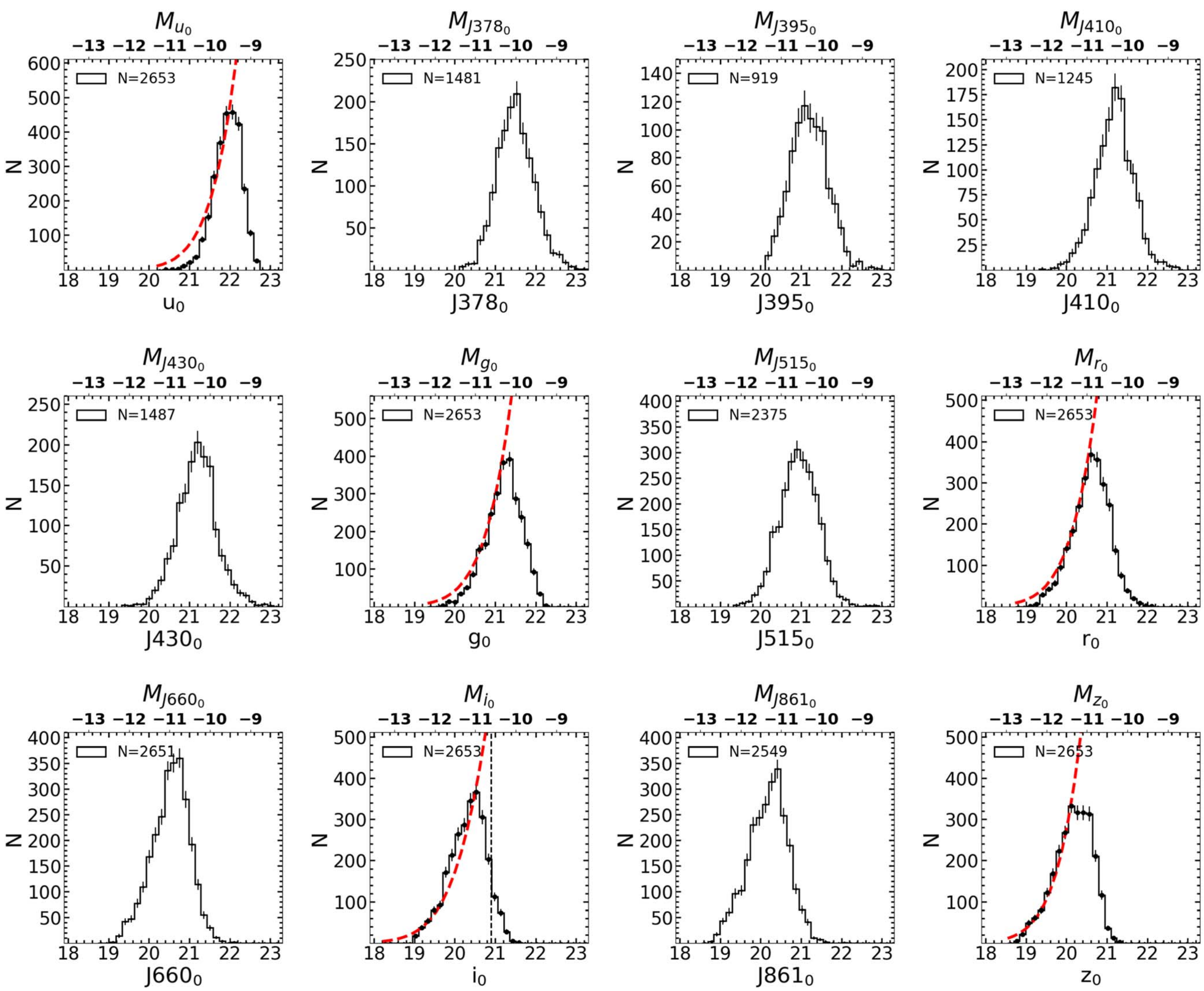

Figure 18. Same color code as in Figure 13.

ORCID iDs

Luis Lomelí-Núñez https://orcid.org/0000-0003-2127-2841
A. Cortesi https://orcid.org/0000-0002-0620-136X
A. V. Smith Castelli https://orcid.org/0009-0007-2396-0003
M. L. Buzzo https://orcid.org/0000-0003-3153-8543
Y. D. Mayya https://orcid.org/0000-0002-4677-0516
Vasiliki Fragkou https://orcid.org/0000-0002-8634-4204
J. A. Alzate-Trujillo https://orcid.org/0000-0002-8351-8854
R. F. Haack https://orcid.org/0009-0005-6830-1832
J. P. Calderón https://orcid.org/0000-0003-2931-2932
A. R. Lopes https://orcid.org/0000-0002-6164-5051
Michael Hilker https://orcid.org/0000-0002-2363-5522
M. Grossi https://orcid.org/0000-0003-4675-3246
Ana L. Chies-Santos https://orcid.org/0000-0003-3220-0165
L. A. Gutiérrez-Soto https://orcid.org/0000-0002-9891-8017
Ciria Lima-Dias https://orcid.org/0009-0006-0373-8168
S. V. Werner https://orcid.org/0000-0002-7186-7889
Pedro K. Humire https://orcid.org/0000-0003-3537-4849
R. C. Thom de Souza https://orcid.org/0000-0003-2435-8528
A. Alvarez-Candal https://orcid.org/0000-0002-5045-9675
Swayamtrupta Panda https://orcid.org/0000-0002-5854-7426
Avinash Chaturvedi https://orcid.org/0000-0002-4175-4728
E. Telles https://orcid.org/0000-0002-8280-4445
C. Mendes de Oliveira https://orcid.org/0000-0002-5267-9065
T. Ribeiro https://orcid.org/0000-0002-0138-1365
W. Schoenell https://orcid.org/0000-0002-4064-7234

References

Alamo-Martínez, K. A., & Blakeslee, J. P. 2017, ApJ, 849, 6
Alamo-Martínez, K. A., Blakeslee, J. P., Jee, M. J., et al. 2013, ApJ, 775, 20
Alves-Brito, A., Hau, G. K. T., Forbes, D. A., et al. 2011, MNRAS, 417, 1823
Annibali, F., Morandi, E., Watkins, L. L., et al. 2018, MNRAS, 476, 1942
Arnouts, S., Moscardini, L., Vanzella, E., et al. 2002, MNRAS, 329, 355
Ashman, K. M., & Zepf, S. E. 1992, ApJ, 384, 50
Ashman, K. M., & Zepf, S. E. 1998, CAS, 30
Barmby, P., Kuntz, K. D., Huchra, J. P., & Brodie, J. P. 2006, AJ, 132, 883
Bassino, L. P., Cellone, S. A., Forte, J. C., & Dirsch, B. 2003, A&A, 399, 489
Bassino, L. P., Richtler, T., & Dirsch, B. 2006, MNRAS, 367, 156
Bastian, N., Adamo, A., Gieles, M., et al. 2011, MNRAS, 417, L6
Beasley, M. A. 2020, Reviews in Frontiers of Modern Astrophysics; From Space Debris to Cosmology, 245
Bergond, G., Athanassoula, E., Leon, S., et al. 2007, A&A, 464, L21
Bertin, E. 2011, in ASP Conf. Ser. 442, Astronomical Data Analysis Software and Systems XX, ed. I. N. Evans et al. (San Francisco, CA: ASP), 435
Bertin, E., & Arnouts, S. 1996, A&AS, 117, 393
Bessell, M. S. 1990, PASP, 102, 1181
Bica, E., Dutra, C. M., Soares, J., & Barbuy, B. 2003, A&A, 404, 223
Blakeslee, J. P., Cho, H., Peng, E. W., et al. 2012, ApJ, 746, 88
Blakeslee, J. P., Jordán, A., Mei, S., et al. 2009, ApJ, 694, 556
Bom, C. R., Cortesi, A., Ribeiro, U., et al. 2024, MNRAS, 528, 4188
Brodie, J. P., & Strader, J. 2006, ARA&A, 44, 193
Bruzual, G., & Charlot, S. 2003, MNRAS, 344, 1000
Burkert, A., & Forbes, D. A. 2020, AJ, 159, 56
Burkert, A., & Tremaine, S. 2010, ApJ, 720, 516
Buzzo, M. L., Cortesi, A., Forbes, D. A., et al. 2022, MNRAS, 510, 1383
Cantiello, M., D'Abrusco, R., Spavone, M., et al. 2018, A&A, 611, A93
Cardelli, J. A., Clayton, G. C., & Mathis, J. S. 1989, ApJ, 345, 245
Caso, J. P., Ennis, A. I., & De Bórtoli, B. J. 2024, MNRAS, 527, 6993
Cenarro, A. J., Moles, M., Cristóbal-Hornillos, D., et al. 2019, A&A, 622, A176
Chaturvedi, A., Hilker, M., Cantiello, M., et al. 2022, A&A, 657, A93
Cohen, J. G. 1988, AJ, 95, 682
Côté, P., Blakeslee, J. P., Ferrarese, L., et al. 2004, ApJS, 153, 223
Côté, P., Marzke, R. O., & West, M. J. 1998, ApJ, 501, 554
D'Abrusco, R., Cantiello, M., Paolillo, M., et al. 2016, ApJL, 819, L31
D'Abrusco, R., Zegeye, D., Fabbiano, G., et al. 2022, ApJ, 927, 15
Dawe, J. A., & Dickens, R. J. 1976, Natur, 263, 395
DESI Collaboration, Adame, A. G., Aguilar, J., et al. 2024, AJ, 168, 58
Diego, J. M., Pascale, M., Frye, B., et al. 2023, A&A, 679, A159
Dirsch, B., Richtler, T., Geisler, D., et al. 2003, AJ, 125, 1908
Drinkwater, M. J., Gregg, M. D., & Colless, M. 2001, ApJL, 548, L139
Durrell, P. R., Côté, P., Peng, E. W., et al. 2014, ApJ, 794, 103
Eigenthaler, P., Puzia, T. H., Taylor, M. A., et al. 2018, ApJ, 855, 142
Euclid Collaboration, Scaramella, R., Amiaux, J., et al. 2022, A&A, 662, A112
Fahrion, K., Lyubenova, M., Hilker, M., et al. 2020, A&A, 637, A27
Federle, S., Gómez, M., Mieske, S., et al. 2024, arXiv:2406.08635
Fedotov, K., Gallagher, S. C., Konstantopoulos, I. S., et al. 2011, AJ, 142, 42
Fensch, J., Mieske, S., Müller-Seidlitz, J., & Hilker, M. 2014, A&A, 567, A105
Ferrarese, L., Côté, P., Cuillandre, J.-C., et al. 2012, ApJS, 200, 4
Forbes, D. A., Bastian, N., Gieles, M., et al. 2018a, RSPSA, 474, 20170616
Forbes, D. A., Read, J. I., Gieles, M., & Collins, M. L. M. 2018b, MNRAS, 481, 5592
Forbes, D. A., & Remus, R.-S. 2018, MNRAS, 479, 4760
Gaia Collaboration, Brown, A. G. A., Vallenari, A., et al. 2021, A&A, 650, C3
Gaia Collaboration, Prusti, T., de Bruijne, J., H., J., et al. 2016, A&A, 595, A1
Gallagher, S. C., Durrell, P. R., Elmegreen, D. M., et al. 2010, AJ, 139, 545
Gebhardt, K., & Kissler-Patig, M. 1999, AJ, 118, 1526
Georgiev, I. Y., Hilker, M., Puzia, T. H., et al. 2006, A&A, 452, 141
Georgiev, I. Y., Puzia, T. H., Goudfrooij, P., & Hilker, M. 2010, arXiv:1010.3228
González-Lópezlira, R. A., Lomelí-Núñez, L., Álamo-Martínez, K., et al. 2017, ApJ, 835, 184
González-Lópezlira, R. A., Lomelí-Núñez, L., Ordenes-Briceño, Y., et al. 2022, ApJ, 941, 53
González-Lópezlira, R. A., Mayya, Y. D., Loinard, L., et al. 2019, ApJ, 876, 39
Graham, A. W., Colless, M. M., Busarello, G., Zaggia, S., & Longo, G. 1998, A&AS, 133, 325
Haack, R. F., Smith Castelli, A. V., Mendes de Oliveira, C., et al. 2024, MNRAS, 530, 3195
Hanes, D. A. 1977, MmRAS, 84, 45
Hanes, D. A., & Harris, W. E. 1986, ApJ, 309, 564
Hargis, J. R., & Rhode, K. L. 2014, ApJ, 796, 62
Harris, G. L. H., & Harris, W. E. 2011, MNRAS, 410, 2347
Harris, W. E. 1987, ApJL, 315, L29
Harris, W. E. 1991, ARA&A, 29, 543
Harris, W. E. 1996, AJ, 112, 1487
Harris, W. E. 2010, arXiv:1012.3224
Harris, W. E., Harris, G. L. H., & Alessi, M. 2013, ApJ, 772, 82
Harris, W. E., Morningstar, W., Gnedin, O. Y., et al. 2014, ApJ, 797, 128
Harris, W. E., & Reina-Campos, M. 2024, arXiv:2404.10813
Harris, W. E., & van den Bergh, S. 1981, AJ, 86, 1627
Herpich, F. R., Almeida-Fernandes, F., Oliveira Schwarz, G. B., et al. 2024, arXiv:2407.20701
Hudson, M. J., Harris, G. L., & Harris, W. E. 2014, ApJL, 787, L5
Hwang, N., & Lee, M. G. 2008, AJ, 135, 1567
Iodice, E., Capaccioli, M., Grado, A., et al. 2016, ApJ, 820, 42
Johnston, E. J., Puzia, T. H., D'Ago, G., et al. 2020, MNRAS, 495, 2247
Jones, C., Stern, C., Forman, W., et al. 1997, ApJ, 482, 143
Jordán, A., Côté, P., Blakeslee, J. P., et al. 2005, ApJ, 634, 1002
Jordán, A., Peng, E. W., Blakeslee, J. P., et al. 2015, ApJS, 221, 13
Jordán, A., Blakeslee, J. P., Côté, P., et al. 2007a, ApJS, 169, 213
Jordán, A., McLaughlin, D. E., Côté, P., et al. 2007b, ApJS, 171, 101
Jordi, K., Grebel, E. K., & Ammon, K. 2006, A&A, 460, 339
Karim, N., Collins, M. L. M., Forbes, D. A., & Read, J. I. 2024, MNRAS, 530, 4936
Kartha, S. S., Forbes, D. A., Spitler, L. R., et al. 2014, MNRAS, 437, 273
Kaviraj, S., Crockett, R. M., Whitmore, B. C., et al. 2012, MNRAS, 422, L96
Kim, H.-S., Yoon, S.-J., Sohn, S. T., et al. 2013, ApJ, 763, 40
Kissler-Patig, M., Brodie, J. P., Schroder, L. L., et al. 1998, AJ, 115, 105
Kissler-Patig, M., Kohle, S., Hilker, M., et al. 1997, A&A, 319, 470
Kluge, M., Hatch, N. A., Montes, M., et al. 2024, arXiv:2405.13503
Kron, R. G. 1980, ApJS, 43, 305
Kruijssen, J. M. D., Pfeffer, J. L., Reina-Campos, M., Crain, R. A., & Bastian, N. 2019, MNRAS, 486, 3180
Kundu, A., & Whitmore, B. C. 1998, AJ, 116, 2841
Larsen, S. S. 2002, AJ, 124, 1393
Larsen, S. S., & Brodie, J. P. 2003, ApJ, 593, 340
Larsen, S. S., Brodie, J. P., Huchra, J. P., Forbes, D. A., & Grillmair, C. J. 2001, AJ, 121, 2974
Lee, M. G., Bae, J. H., & Jang, I. S. 2022, ApJL, 940, L19
Lomelí-Núñez, L., Mayya, Y. D., Rodríguez-Merino, L. H., Ovando, P. A., & Rosa-González, D. 2022, MNRAS, 509, 180
Maddox, N., Serra, P., Venhola, A., et al. 2019, MNRAS, 490, 1666
Mayya, Y. D., Romano, R., Rodríguez-Merino, L. H., et al. 2008, ApJ, 679, 404
McLaughlin, D. E., Harris, W. E., & Hanes, D. A. 1994, ApJ, 422, 486

Mendes de Oliveira, C., Ribeiro, T., Schoenell, W., et al. 2019, MNRAS, 489, 241
Mieske, S., Jordán, A., Côté, P., et al. 2010, ApJ, 710, 1672
Minniti, D., Kissler-Patig, M., Goudfrooij, P., & Meylan, G. 1998, AJ, 115, 121
Muñoz, R. P., Eigenthaler, P., Puzia, T. H., et al. 2015, ApJL, 813, L15
Muñoz, R. P., Puzia, T. H., Lançon, A., et al. 2014, ApJS, 210, 4
Muratov, A. L., & Gnedin, O. Y. 2010, ApJ, 718, 1266
Ordenes-Briceño, Y., Puzia, T. H., Eigenthaler, P., et al. 2018, ApJ, 860, 4
Ostrov, P. G., Forte, J. C., & Geisler, D. 1998, AJ, 116, 2854
Peacock, M. B., Maccarone, T. J., Knigge, C., et al. 2010, MNRAS, 402, 803
Peng, E. W., Jordán, A., Côté, P., et al. 2006, ApJ, 639, 95
Peng, E. W., Jordán, A., Côté, P., et al. 2008, ApJ, 681, 197
Pickles, A. J. 1998, PASP, 110, 863
Pota, V., Forbes, D. A., Romanowsky, A. J., et al. 2013, MNRAS, 428, 389
Pota, V., Romanowsky, A. J., Brodie, J. P., et al. 2015, MNRAS, 450, 3345
Powalka, M., Puzia, T. H., Lançon, A., et al. 2018, ApJ, 856, 84
Prole, D. J., Hilker, M., van der Burg, R. F. J., et al. 2019, MNRAS, 484, 4865
Reed, L. G., Harris, G. L. H., & Harris, W. E. 1994, AJ, 107, 555
Reina-Campos, M., Trujillo-Gomez, S., Deason, A. J., et al. 2022, MNRAS, 513, 3925
Reina-Campos, M., Trujillo-Gomez, S., Pfeffer, J. L., et al. 2023, MNRAS, 521, 6368
Richtler, T. 2003, LNP, 635, 281
Robin, A. C., Reylé, C., Derrière, S., & Picaud, S. 2003, A&A, 409, 523
Saifollahi, T., Voggel, K., Lançon, A., et al. 2024, arXiv:2405.13500
Schlafly, E. F., & Finkbeiner, D. P. 2011, ApJ, 737, 103
Schuberth, Y., Richtler, T., Bassino, L., & Hilker, M. 2008, A&A, 477, L9
Schuberth, Y., Richtler, T., Hilker, M., et al. 2010, A&A, 513, A52
Scoville, N., Abraham, R. G., Aussel, H., et al. 2007, ApJS, 172, 38
Serra, P., Maccagni, F. M., Kleiner, D., et al. 2023, A&A, 673, A146
Sifón, C., Finoguenov, A., Haines, C. P., et al. 2024, arXiv:2411.13655
Simanton, L. A., Chandar, R., & Whitmore, B. C. 2015, ApJ, 805, 160
Smith Castelli, A. V., Cortesi, A., Haack, R. F., et al. 2024, MNRAS, 530, 3787
Spitler, L. R., & Forbes, D. A. 2009, MNRAS, 392, L1
Strader, J., Brodie, J. P., Cenarro, A. J., Beasley, M. A., & Forbes, D. A. 2005, AJ, 130, 1315
Tody, D. 1986, Proc. SPIE, 627, 733
van den Bergh, S., Morbey, C., & Pazder, J. 1991, ApJ, 375, 594
Venhola, A., Peletier, R., Laurikainen, E., et al. 2019, A&A, 625, A143
Villegas, D., Jordán, A., Peng, E. W., et al. 2010, ApJ, 717, 603
Voggel, K. T., Seth, A. C., Sand, D. J., et al. 2020, ApJ, 899, 140
Wang, S., Ma, J., & Liu, J. 2019, A&A, 623, A65
Webb, J. J., Harris, W. E., & Sills, A. 2012, ApJL, 759, L39
West, M. J., Cote, P., Jones, C., Forman, W., & Marzke, R. O. 1995, ApJL, 453, L77
West, M. J., Côté, P., Marzke, R. O., & Jordán, A. 2004, Natur, 427, 31
White, R. E. I. 1987, MNRAS, 227, 185
Whitmore, B. C., Chandar, R., Lee, J. C., et al. 2023, arXiv:2301.03689
Whitmore, B. C., Chandar, R., Bowers, A. S., et al. 2014, AJ, 147, 78
Whitmore, B. C., Sparks, W. B., Lucas, R. A., Macchetto, F. D., & Biretta, J. A. 1995, ApJL, 454, L73
Whitmore, B. C., Zhang, Q., Leitherer, C., et al. 1999, AJ, 118, 1551
Williams, B. F., Ciardullo, R., Durrell, P. R., et al. 2007, ApJ, 654, 835
Zaritsky, D., Donnerstein, R., Dey, A., et al. 2023, ApJS, 267, 27
Zepf, S. E., & Ashman, K. M. 1993, MNRAS, 264, 611
Zhang, H.-X., Peng, E. W., Côté, P., et al. 2015, ApJ, 802, 30